Volume 5, Issue 3, 2019

Journal of Biomedical Photonics & Engineering

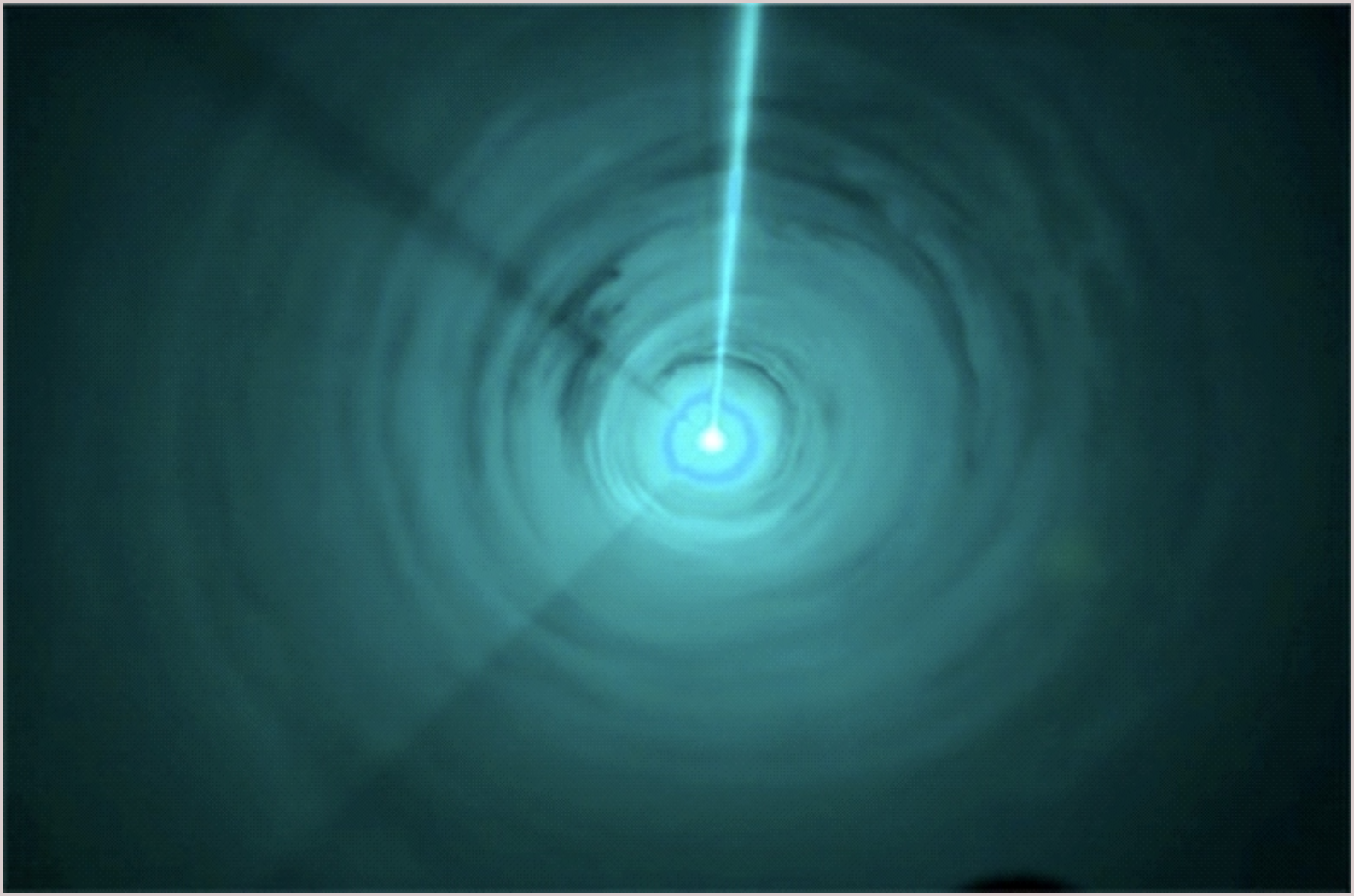

 doi: 10.18287/JBPE18.05.030001

Journal of Biomedical Photonics & Engineering

by Samara National Research University

Volume 5, Issue 3 (September 2019)

Editorial Board

Postal address:
39B Lukacheva st., room #301
Samara 443086, Russian Federation

Contents

Articles

Capabilities of Autodyne Reception in Medical CO_2 Laser Devices

Alexandr K. Dmitriev, Alexey N.Konovalov*, Vladimir N. Kortunov, and Valerii A. Ulyanov
Institute of Photon Technologies of Federal Scientific Research Centre "Crystallography and Photonics" of Russian Academy of Sciences, 2 Pionerskaya str., Moscow, Troitsk 108840, Russian Federation

*** e-mail:** ank27.ift@mail.ru

Abstract. The generation characteristics and the capabilities of autodyne reception in single mode CO_2 lasers with pulse-periodic pumping of the active medium used in medical laser devices are investigated. It has been demonstrated that medical laser device based on CO_2 laser model DIAMOND C-30A (Coherent Co.) has the best long-term laser power stability ((2–3)%), while the setup with CO_2 laser model 48–2W (Synrad Co.) has the best short-term stability (0.62%). Amplitude-frequency characteristics of autodyne reception were studied for lasers of these devices. Power spectra of the autodyne signal appearing during evaporation of fat and muscle tissues under CO_2 laser radiation of the three types of laser devices were recorded. It has been shown that all these laser devices allow to detect the autodyne signal during evaporation of biological tissues. The medical laser setup with CO_2 laser model 48–2W has the highest signal-to-noise ratio during detection of laser backscattered radiation. This is due to the fact that this laser has larger autodyne amplification and better short-term power stability. The results can be used in the development of smart laser surgical systems with feedback.

Keywords: medical laser device; CO2 laser; laser power stability; autodyne reception; signal-to-noise ratio; laser evaporation; biotissues.

Paper #3321 received 29 Mar 2019; revised manuscript received 10 Jun 2019; accepted for publication 10 Jul 2019; published online 1 Aug 2019. doi: 10.18287/JBPE19.05.030301.

1 Introduction

The creation of the so-called smart laser medical systems is a modern development trend of laser medicine. Setting up feedback is the key problem in creation of such systems. The feedback should not only allow to visualize the surgical area and to remotely manipulate in it (this can be done using the existing modern methods of image acquisition and transfer and the corresponding technical equipment), but also to receive objective information about the process of surgical intervention and to make automated decisions on changing the conditions of operation [1, 2].

Currently, the vision and experience of the surgeon play the role of "peripheral sensors" and "database" in the feedback system when laser operations are conducted. Such feedback does not always guarantee the full removal of diseased tissues and minimum damage of healthy tissues, does not exclude human factor risks and does not allow to evaluate objectively the quality of the operation performed. Such advantages of the laser scalpel as high speed of removal of diseased tissues, precision, low invasiveness will be most fully realized if feedback is introduced into the composition of laser surgical systems for the purpose of real-time supervision and control over the process of laser intervention.

Surgical devices based on single-mode CO_2 lasers with a radiation wavelength of 10.6 μm are widely used [3] in medical practice. In order to diagnose and control the process of laser surgical intervention in real time, we have suggested [4–7] an approach based on the self-heterodyne method for such devices, wherein the operating laser radiation is simultaneously a diagnostic one, creating an optical information feedback channel. The essence of the method is that the backscatter from the moving exterior object reaches the laser cavity and initiates a modulation of the laser output power

(autodyne signal) at the Doppler frequency. This process is called the autodyne effect in lasers [8]. The modulation of the laser power arises due to the mixing in the laser cavity of the main radiation and backscattered frequency-shifted radiation. This is similar to optical heterodyning. Therefore, this effect is sometimes called self-heterodyning and self-mixing [4, 6]. The operational diagnostics of processes of laser evaporation of biological tissues in accordance with this method consists in discovering discrepancies and distinctive features of amplitude and frequency characteristics of the signal for different types of evaporated biological tissues and correcting the parameters of applied laser radiation [4–7]. This self-heterodyne process has been well studied for continuous CO_2 lasers [6]. The paper [6] presents a theoretical model of the autodyne effect in CO_2 lasers of this type, describing the amplitude-frequency characteristics (AFC) of autodyne amplification, modulation depth and non-linear signal distortions of the autodyne signal at high levels of backscatter/reflection. It has been shown that the original spectrum of the Doppler backscattering signal can be reconstructed from the autodyne signal spectrum when the "weak" backscattered signal is realized. It is demonstrated that a weak Doppler backscattering signal is formed during CO_2 laser radiation interaction with organic materials, which does not introduce nonlinear distortions into the autodyne signal [6]. Thus, this method can be used to receive real-time information and diagnose the process of laser evaporation/dissection of biological tissues. In our proposed approach to creating an optical information feedback channel, a surgical CO_2 laser is simultaneously a diagnostic one. In this regard, as for any laser Doppler diagnostic methods, the corresponding requirements for mode structure and radiation stability are imposed on this laser. At the same time, CO_2 lasers pumped with trains of radio frequency (RF) pulses (with frequency ranging from tens to hundreds of MHz) with variable pulse ratio (hereinafter – pulse-periodic (PP) pumping) are often used in surgical devices. These lasers are characterized by compactness, long-term stability of operating characteristics and long life-cycle. In these lasers, the "continuous" laser radiation is a pulse train with a frequency of 5–20 kHz, where laser power is modified by changing the pump pulse duration [9]. A computational model of the self-heterodyne effect in such lasers has earlier been proposed [4]. However, there is no information about the features of use of real surgical devices with this type of lasers as feedback sensors.

This paper presents the results of study of lasing characteristics and the possibilities of autodyne reception in single mode CO_2 lasers with pulse-periodic pumping of the active medium, used in medical laser devices.

2 Materials and Methods

The following medical laser devices were used in order to measure the lasing characteristics and autodyne reception in single mode CO_2 lasers with PP pumping of the active medium:

1. "Lantset" series device (OOO "RIK", Russia) based on a waveguide laser with output up to 25 W [10] (hereinafter as LD-1);
2. "L`med. " series device (OOO "RIK", Russia) [11] based on a CO_2 laser model DIAMOND C-30A [12] produced by Coherent Co. USA (hereinafter as LD-2). Laser output up to 30 W;
3. Medical laser setup based on a CO_2 laser model 48-2W [13] produced by Synrad Co. USA (hereinafter as LD-3). Laser output up to 25 W. UC-2000 Laser Controller from Synrad Co. and MCS20-230/24 power supply from MURR Elektronik Co. were used in this setup.

Studies of the characteristics of CO_2 lasers in these devices were carried out in accordance with the scheme shown in Fig. 1. Laser radiation was focused through a ZnSe lens (focal length of 125 mm, focused laser beam diameter of 400 μm) on the surface of the object of study (a rotating metallic disc or a sample of biological tissue). A part of the radiation (2%) was directed by means of beam splitter to the receiving area of the IR photodetector. A non-cooled fast-response HgCdTe sensor with an integrated preamplifier was used as the photodetector. An electric signal is formed on the photodetector's output in the form of beats at the difference frequency, the spectrum of which is uniquely determined by the spectrum of the scattered light. The signal from the photodetector is directed to the 1-st channel of the fast-response analog-to-digital converter (ADC) ADM212x60M (AO "Instrument systems", Russia). The synchronization pulses from the laser control system were fed to the second ADC channel. Precision power supply device GPC-303DQ was used to provide the laser radiation photodetector with constant current within the (0.5–30) V voltage range and (0.005–3) A current with pulsation below 1 mW. MAESTRO laser power/energy meter with UP19K-30H5-D0 (Gentec-EO, Canada) thermopile power detector was used to measure the output laser power and its long-term stability.

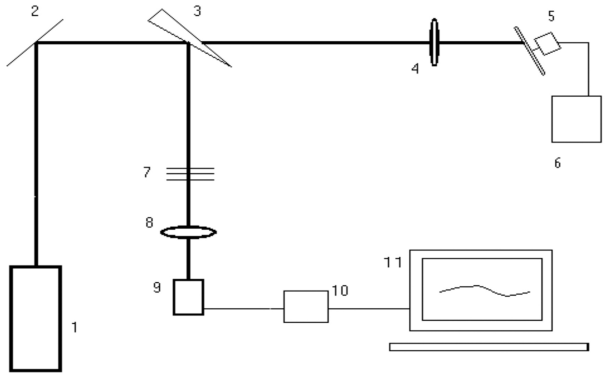

Fig. 1 Schematic diagram of the experimental setup. 1 – CO_2 LD; 2 – copper mirror; 3 – beam splitter; 4 – lens; 5 – rotating metallic disc; 6 – power supply; 7 – teflon attenuators; 8 – lens; 9 – HgCdTe photodetector; 10 – ADC; 11 – PC.

The following studies were performed on the test bench:

- lasing characteristics of undisturbed radiation, including: the shape and amplitude of laser pulses, their repeatability within a short time period (so-called "short-term stability"); the long-term-stability of the laser power; The long-term laser power stability was measured for 10 min, which corresponds to the average time of a laser operation [14]. Long-term stability Δ_{long} was determined using the formula: $\Delta_{long} = \left(P_{\max} - P_{\min}\right) / 2 < P >$, where $P_{\max}$ and $P_{\min}$ are the maximum and minimum lasing power during 10 min of the laser's activity, $<P>$ is the average lasing power during 10 min. Short-term laser power stability was determined as deviation of laser power from the power of the average pulse shape. A special algorithm described in the "Results and Discussion" section was developed to characterize the short-term laser power stability;
- amplitude-frequency characteristics (AFC) of autodyne reception of selected CO_2 lasers using the surface of a rotating disk as a source of backscattered radiation;
- biological models *in vitro* were used to model the process of laser dissection of biological tissues. In surgical practice, this process is performed by moving the focused laser beam along the surface of the biological tissue at a speed of 0.1–10 mm/s. We used a motorized linear translator in our experiments to model the dissection of biological models. Fresh pig tissue samples containing muscle and fat components were placed on it. The samples were steadily moved in relation to the laser beam focused on the samples' surface. Simultaneously, autodyne signal from the products of laser destruction of biological tissues was registered at an average power level of 6.5–7 W for all three laser devices.

All measurements were conducted using the following ADC settings: sampling frequency 7.5 MHz; buffer size – 32768 points. The main method for analyzing an autodyne signal is spectral analysis based on the Fast Fourier Transform (FFT) algorithm.

3 Results and Discussion

The radiation of studied lasers is a sequence of pulses with a repetition frequency of around 10 kHz. Average laser power is regulated by the duration of its pumping pulses. Fig. 2 demonstrates the dynamics of the laser radiation of the LD-2 at average output power of 5 W. The long-term stability of the radiation power of the lasers under study has been measured within 10 min after the laser was switched on.

As an example, the dependency of laser power of LD-3 on time at different relative pulse duration (different average output power) is demonstrated in Fig. 3. Table 1 shows the results of measurement of long-term stability of the laser devices under study.

As follows from Table 1, the best long-term laser power stability (2–3%) was shown by laser model DIAMOND C-30A, being a component of LD-2. The long-term laser power instability in CO_2 laser devices, in general, depends on the design features of the lasers and the lasing conditions at different pumping levels of the lasing medium. These features may include: composition of the working mixture, thermal conditions forming within the laser during long-term activity, possible changes during transition from one lasing line to another (CO_2 laser signature [14]), etc.

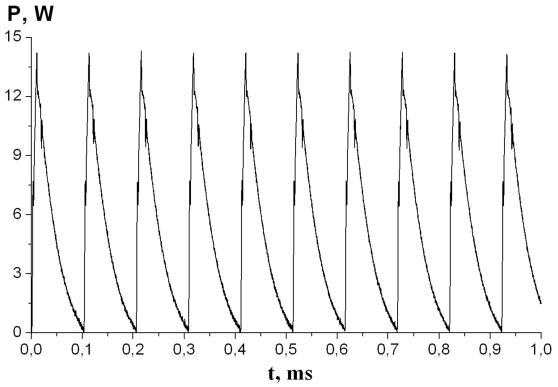

Fig. 2 The dynamics of the laser radiation of the LD-2 at average output power of 5 W.

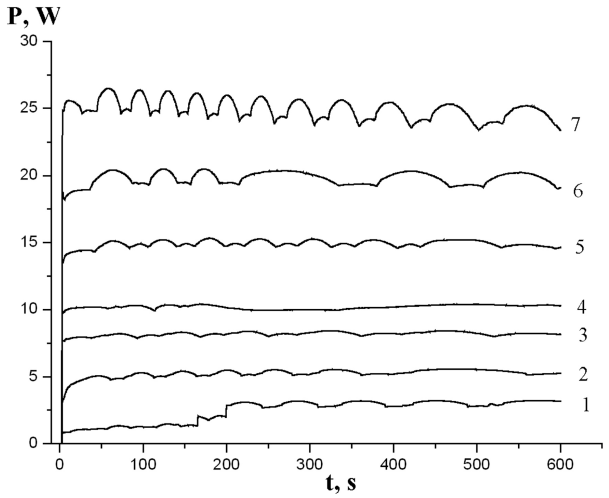

Fig. 3 Long-term instability of the radiation power of the LD-3. 1) P = 3 W; 2) P = 5 W; 3) P = 8 W; 4) P = 10 W; 5) P = 15 W; 6) P = 10 W; 7) P = 25 W.

It is known that the noise characteristics of the laser source are an important parameter for the task of Doppler measurements using CW lasers [15]. These characteristics describe the instability of laser radiation at time intervals during which the signal is registered. This parameter is characterized either by the laser's spectral noise density or the short-term instability. In our case, laser radiation is already modulated at a frequency of around 10 kHz. This is why we cannot directly implement the approaches used for continuous pumping lasers. In this case, the change of the laser pulse shape should be regarded as the laser's noise.

Table 1 Long-term power stability of CO2 lasers of laser devices under study.

Power, W	Long-term laser power stability, +/- SP, %		
	LD-1	LD-2	LD-3
5	2.7	2.6	4.9
10	3.3	2.1	1.3
15	3.1	2.7	3.3
20	10.0	3.0	4.6

Table 2 Short-term instability of CO_2 laser pulses at average output power of 5 W.

Laser device	dPpulse, %		M, %	
	5 W	15 W	5 W	15 W
LD-1	1.5±1	0.42±0.05	2.45±0.1	0.87±0.05
LD-2	0.77±0.2	0.4±0.05	1.52±0.05	0.75±0.05
LD-3	0.62±0.1	0.36±0.05	1.58±0.05	0.66±0.05

For example, Fig. 4 shows the dynamics of laser power during 35 μs for several laser pulses N (the 10th, the 20th, the 40th) and the average pulse shape (averaging over 40 pulses) for LD-1, at average output power of 5 W. As demonstrated, a notable instability can be observed in LD-1's laser at the initial time of the pulse and at time interval of 15–25 μs.

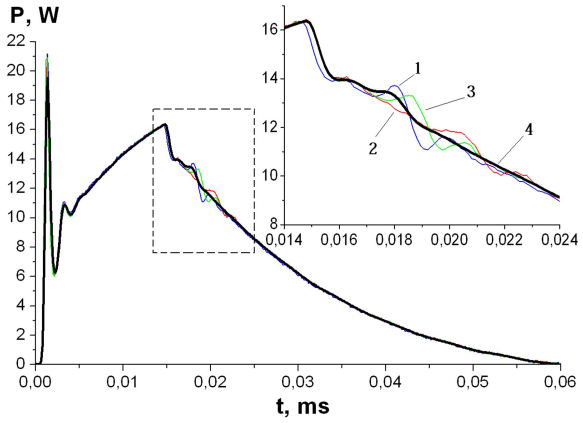

Fig. 4 Dynamics of laser power during 60 μs for several laser pulses of LD-1 radiation. Average radiation power 5W. 1) blue – the 10th pulse; 2) red – the 20th pulse; 3) green – the 40th pulse; 4) black, bold – the average pulse shape.

We shall regard the deviation of laser power from the average pulse shape as the level of short-term laser power instability. We have elaborated an algorithm to characterize this short-term instability of CO_2 lasers with PP pumping. For this we established the average pulse shape $P_0(t)$ during 4.37 ms (ADC selection of 32768 points at sampling frequency of 7.5 MHz). This time interval comprises around 40 pulses produced by CO_2 lasers. After determining the average laser pulse shape we determined the root-mean-square deviation of laser power $P(t)$ from the average pulse shape $P_0(t)$. The short-term laser power instability for these lasers was determined as a ratio of the root-mean-square power deviation from the power of the average pulse shape $P_0(t)$ to the average laser power $\langle P(t)\rangle$:

$$dP_{pulse} = \frac{\sqrt{\left\langle \left(P(t) - P_0(t)\right)^2 \right\rangle}}{\left\langle P(t) \right\rangle}. \qquad (1)$$

Here the angle brackets "< >" mean averaging over the duration of the laser pulse period. Herewith, the dP_{pulse} value may vary from pulse to pulse (Fig. 5). Table 2 shows the results of calculation of short-term instability for the three laser devices at average output power of 5 W and 15 W, averaged across 40 laser pulses.

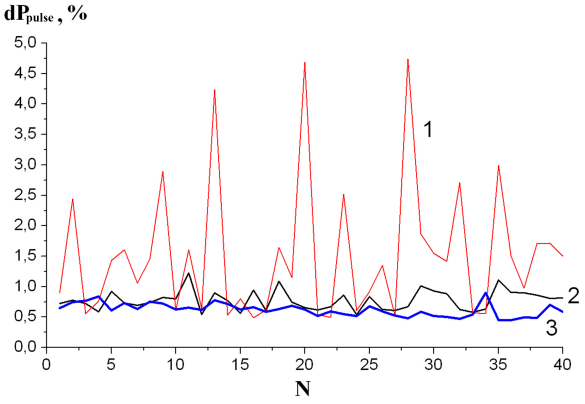

Fig. 5 Short-term laser power instability dP_{pulse}. 1) red – LD-1; 2) black – LD-2; 3) blue – LD-3. Average output power is 5 W.

Note that the larger the short-term stability of laser radiation, the more repetitive are the pulse shapes, and, therefore, smaller autodyne signals, appearing due to backscatter laser radiation, can be revealed. The level of short-term instability determines the minimum autodyne signal that can be detected. Experiments have shown that the LD-3 has the maximum short-term stability. Therefore we suppose that this LD will demonstrate an

autodyne signal with a higher signal/noise ratio. It should be mentioned that when laser power is increased, the short-term instability parameter falls. Moreover, short-term instability is almost similar for LD-1, LD-2 and LD-3 at laser power of 15 W. This is due to two factors. First, when power is increased, laser impulses become smoother. Second, the modulation depth of laser radiation decreases as <*P*> grows. Table 1 shows the modulation depth, determined using the formula $M = \langle (P_{max} - P_{min}) \rangle / 2 < P >$, where P_{max} and P_{min} are the maximum and minimum pulse power, respectively.

When backscatter radiation from a moving object reaches the laser cavity, an additional modulation of laser output power appears at the Doppler frequency. Fig. 6 shows the one laser pulse with autodyne signal on LD-1, received when radiation was scattered by the rotating disk at laser power of 7 W. The level of autodyne signal depends both on the backscatter coefficient and the autodyne amplification [4, 6].

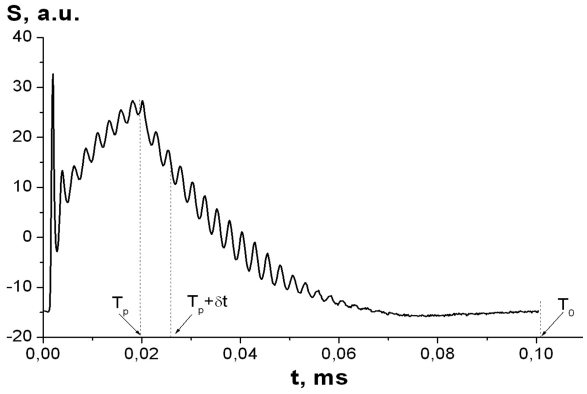

Fig. 6 Autodyne signal on LD-1, received when radiation was scattered by the rotating disk. Average output power is 7 W.

In order to measure the amplitude-frequency characteristics (AFC) of autodyne amplification of the lasers, we used an algorithm that allowed to extract the variable component from the laser pulses due to the autodyne effect. The algorithm suggests subtracting the average laser pulse, recorded in the absence of the rotating disk, from the registered signal. Thus, the newly obtained signal only contains the variable component at the Doppler frequency, as well as a component caused by the irreproducibility of the laser pulse shapes (short-term instability). The latter was mostly observed at the initial stage of the pulse and near the part of the beginning of the decline (see Fig.4). We further determined a time slot $t_p + \delta t < t < T_0 - \delta t$ (T_0 is the time period of the laser's amplitude modulation, t_p is the pump pulse duration, see Fig. 6) on the rear falling edge of the pulse and found the signal power spectrum within the selected time slot, averaged across 40 periods. Fig. 7 shows the power spectrum of autodyne signal in the CO_2 LD-3 (P = 6.7 W) during scattering from the surface of the disk rotating at a constant speed.

We measured the frequency response of the autodyne detection for all CO_2 laser devices, which was determined as the dependence of the area of the power spectrum of autodyne signal on the Doppler frequency shift. The area of the power spectrum was determined in the spectral window $\nu_0 - d\nu < \nu_0 < \nu_0 + d\nu$ (ν_0 is the spectrum peak position, $d\nu$= 70 kHz), which obviously exceeds the width of the carrier frequency of the Doppler signal in the whole range of measured frequencies. The results of these measurements are shown in Fig. 8. The measurements for the three CO_2 laser devices were conducted in identical conditions. Laser power during AFC measurements was at 7 W. Herewith, the position of the disk's surface relative to the incident laser beam and the ADC selection parameters were identical.

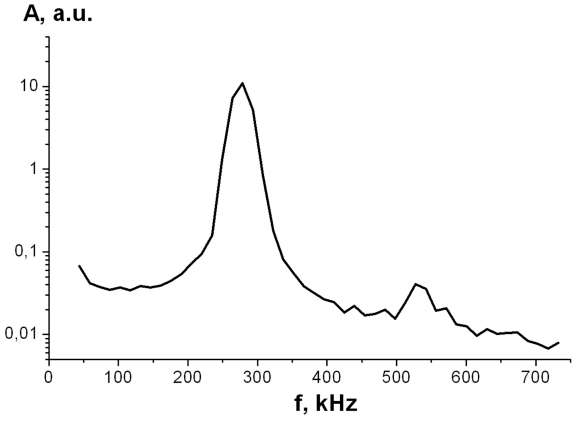

Fig. 7 Power spectrum of autodyne signal in the CO_2 LD-3 during scattering from the surface of the rotating disk. Average output power is 6.7 W.

As follows from Fig. 8, the CO_2 LD-3 has the maximum autodyne amplification. Greater autodyne amplification means that this laser is more sensitive to backscatter. It should also be pointed out that the maximum of the AFC resonance curve for this laser is located at lower frequencies. This is also more optimal from the viewpoint of detecting the autodyne signal appearing during scattering from biological tissues during their laser evaporation. This is due to the fact that the original spectrum of the Doppler backscatter signal during laser evaporation of biological tissues is located near the low frequencies [6, 7].

We conducted studies detecting the autodyne signal that appears during evaporation of fat and muscle tissues by CO_2 lasers devices. The biological tissue samples were placed on the moving stage. It moved the sample within the focal plane of the lens 4 (Fig. 1) in a direction perpendicular to the optical axis. Movement speed V was constant and equaled 0.75 mm/s. Laser power was at 6.7 ± 0.2 W. Fig. 9a shows the averaged power spectra of the autodyne signal formed in the CO_2 LD-3 during evaporation of fat and muscle tissues by laser radiation at output power of 6.7 W. Fig. 9b shows the averaged power spectra of autodyne signals after subtracting the noise power spectrum. As we

demonstrated in Ref. [16], the power spectra of the autodyne signal depend on the features of laser induced mass transfer within the area of laser interaction with tissues, as well as the quantity, size and dynamic characteristics of diffusers. In particular, the nature of mass removal during laser evaporation of biological tissues is defined by their structural features and water content (20–40% of water for fat tissues and 70% for muscle tissues [16]), which determine the absorption capacity of the tissue at CO_2 laser wavelength $\lambda = 10.6$ μm. A significant change in water content leads to a change in the tissue destruction mechanisms: from intensive surface evaporation (as in the case of laser dissection of muscle tissue) to volumetric explosive boiling (in fat tissue).

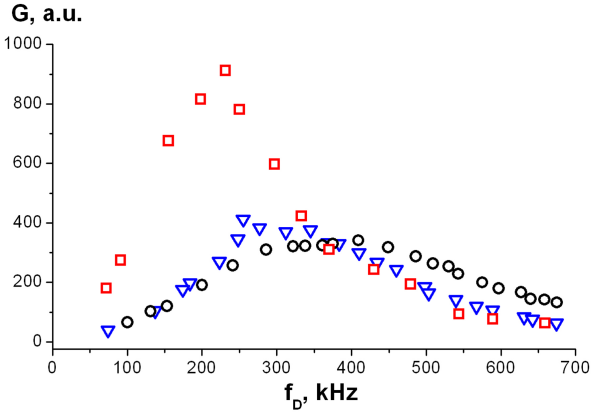

Fig.8 Amplitude-frequency characteristics of autodyne reception. □ (red) – LD-3; O (black) – LD-1; ∇ (blue) – LD-2. Average output power is 7 W.

Surface evaporation produces small (10–50 μm) fragments of tissue structures, moving at a speed around 1 m/s, and water steam. Laser heating of fat tissue leads to overheating and explosive boiling of the water located within the tissues, followed by ejection of large (up to 300 μm) drops of water and fat. This is accompanied by an apparent increase of the autodyne signal power, which is well demonstrated in Fig. 9. Herewith, as seen in Fig. 9b, the nature of the form of autodyne signal power spectra during dissection of fat and muscle tissues is similar, with a characteristic maximum at a frequency of 150 kHz. This behavior of spectra in different tissues is explained by the fact that the original spectrum of the Doppler backscattered signal overlaps with the AFC of autodyne reception, which has a resonance form with a maximum at a frequency of 230 kHz. A similar picture was earlier observed during continuous CO_2 laser impact on PMMA [6]. Similar differences of spectra of these types of tissues were found for all the laser devices used for the study (see Table 3).

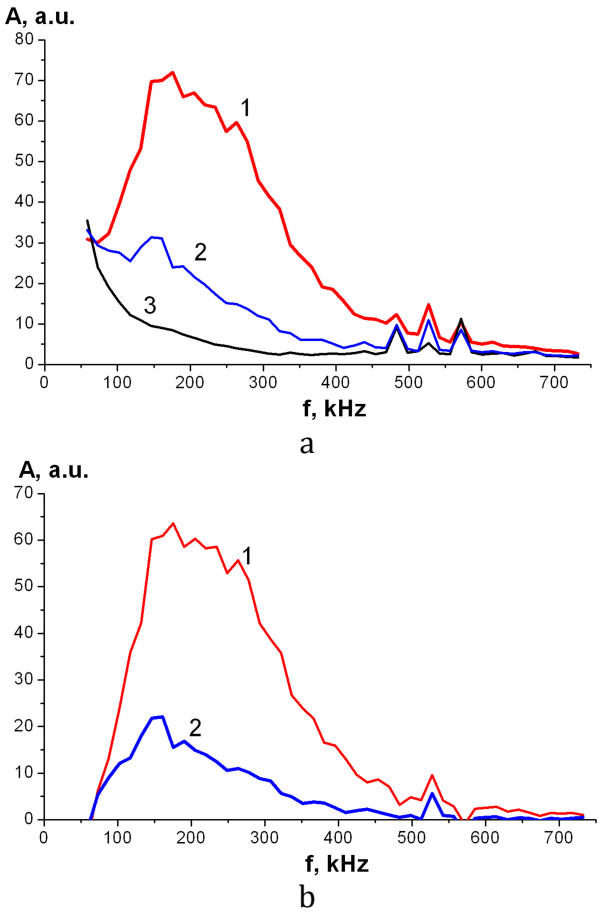

Fig. 9 Averaged power spectra of the autodyne signal formed in the CO_2 LD-3 during evaporation of biotissues. a) power spectra of the original autodyne signals; b) averaged power spectra of autodyne signals after subtracting the noise power spectrum. 1 – fat; 2 – muscle. 3 – noise. Average output power is 6.7 W. V = 0.75 mm/sec.

Table 3 Signal/noise ratio of the autodyne signal in CO_2 LD.

Laser device / **signal/noise**	LD-1 (6.5 W)	LD-2 (6.8 W)	LD-3 (6.7 W)
Disk, max of AFC	350	120	790
muscle	1.7	1.15	2.0
fat	3.1	1.4	3.8

The results of studies of autodyne reception in the CO_2 lasers of the devices are shown in Table 3. Table 3 demonstrates the signal/noise ratio at maximum sensitivity of AFC during scattering of radiation from the rotating disk and the signal/noise ratio within the (70–520) kHz spectral range during evaporation of biological tissues. As can be seen in Table 3, the CO_2 LD-3 has the highest signal-to-noise ratio. This is due to the fact that the LD-3 has a minimum level of short-term instability (Table 2).

4 Conclusions

Studies of the generation characteristics and the capabilities of autodyne reception in CO_2 lasers with PP pumping of the active medium used in medical laser devices are carried out. The best long-term laser power stability (2–3%) was demonstrated by LD-2 with laser model DIAMOND C-30A, produced by Coherent company, while the best short-term stability (0.62%) was demonstrated by LD-3 with CO_2 laser model 48-2W, produced by Synrad company. The amplitude-frequency characteristic of the autodyne reception for these lasers was measured. Power spectra of the autodyne signal appearing during evaporation of fat and muscle tissues by laser radiation were obtained. The experiments have shown that all the lasers under study make it possible to detect the autodyne signal during the evaporation of biological tissues. CO_2 laser 48-2W installed on LD-3 also has the highest signal/noise ratio when detecting laser backscattered radiation. This is due to the fact that this laser has the largest autodyne amplification and the best short-term stability as compared to the lasers installed on LD-1 and LD-2. The results can be used in the development of smart surgical systems based on CO_2 lasers with feedback.

Disclosures

All authors declare that there is no conflict of interests in this paper.

Acknowledgments

This work was supported by the Ministry of Science and Higher Education within the State assignment FSRC “Crystallography and Photonics” RAS in part of “the dynamics of laser evaporation of biotissues” and Russian Science Foundation (Project No. 18-29-02069-мк) in other parts.

References

1. Q. Peng, A. Juzeniene, J. Chen, L. O. Svaasand, T. Warloe, K.-E. Giercksky, and J. Moan, “Lasers in medicine,” Reports on Progress in Physics 71(5), 056701 (2008).
2. A. K. Dmitriev, A. N. Konovalov, V. N. Kortunov, and V. A. Ulyanov, “Smart” laser scalpels for robotic surgery,” Almanac of Clinical Medicine 44(2), 12–18 (2016) [in Russian].
3. V. P. Minaev, “Laser devices for surgery and power therapy: yesterday, today and tomorrow,” Lazernaya medicina 16(3), 57–65 (2012) [in Russian].
4. A. N. Konovalov, V. A. Ul’yanov, “Self-mixing detection of backscattered radiation in single-mode pulse-periodic CO2 lasers,” Applied Optics 51(17), 3900–3906 (2012).
5. A. K. Dmitriev, A. N. Konovalov, V. Y. Panchenko, V. A. Ulyanov, G. A. Varev, A. V. Geynits, O. V. Matorin, I. V. Reshetov, and G. S. Samoshenkov, “New approaches to precision and small-traumatic biotissue evaporation using intellectual laser surgical systems,” Lazernaya medicina 17(1), 4–10 (2013) [in Russian].
6. V. M. Gordienko, A. N. Konovalov, and V. A. Ul'yanov, “Self-heterodyne detection of backscattered radiation in single-mode CO2 lasers,” Quantum Electronics 41(5), 433–440 (2011).
7. V. V. Vasil'tsov, V. M. Gordienko, A. K. Dmitriev, A. N. Konovalov, V. N. Kortunov, V. Y. Panchenko, and V. A. Ul'yanov, “Diagnostics of the laser perforation of biological tissues by the method of autodyne detection of backscattered radiation,” Quantum Electronics 32(10), 891–896 (2002).
8. A. V. Skripal’, D. A. Usanov, V. A. Vagarin, and M. Y. Kalinkin, “Autodyne detection in a semiconductor laser as the external reflector is moved,” Technical Physics 44(1), 66–68 (1999).
9. D. He, D. R. Hall, “A 30-W radio frequency excited waveguide CO2 laser,” Applied Physics Letters 43(8), 726–728 (1983).
10. S. L. Pogorelsky, V. F. Lazukin, V. F. Maiboroda, and A. M. Barmashov, “Single-mode waveguide gas laser,” Proceeding of SPIE 5137, 311–316 (2003).
11. Lmed-1, Russian Engineering Club Ldt.
12. Diamond C-30A, Coherent Inc.
13. 48 Series: 8W - 50W Lasers, SYNRAD, A Novanta Company.
14. A. K. Koval’, V. B. Mironov, “Investigation of CO2 laser signatures,” Soviet Journal of Quantum Electronics 15(11), 1531–1536 (1985).
15. V. M. Gordienko, A. N. Konovalov, N. V. Kravtsov, Y. Y. Putivskii, V. I. Savin, and V. V. Firsov, “Remote Doppler velocimeter based on an Nd3+: YAG chip laser and its application in a study of laser-induced hydrodynamic flows,” Quantum Electronics 28(10), 827–830 (1998).

16. A. K. Dmitriev, S. V. Ivanov, A. N. Konovalov, V. N. Kortunov, A. V. Koshcheev, and V. A. Ul'yanov, "Study of Particle Motion and Backscattering Signal in Plume During Laser Evaporation of Biotissues," Physics of Wave Phenomena 13(1), 15–23 (2005).

Optical Clearing of the Gastric Mucosa Using 40%-glucose Solution

Vadim D. Genin[1,2*], Elina A. Genina[1,2], Sergey V. Kapralov[3], Veniamin A. Grishaev[4], Valery V. Tuchin[1,2,5], Ekaterina N. Lazareva[1,2], and Alexey N. Bashkatov[1,2]

[1] Saratov State University, 83 Astrakhanskaya Str., Saratov 410012, Russia
[2] Tomsk State University, 36 Prosp. Lenina, Tomsk 634050, Russia
[3] Engels City Clinical Hospital No. 1, 6 Vesennyaya Str., Engels, Saratov Region 413116, Russia
[4] Saratov City Clinical Hospital No. 6 named after Acad. Koshelev, 15 Gvardeyskaya Str., Saratov 410033, Russia
[5] Laboratory of Laser Diagnostics of Technical and Living Systems, Institute of Precision Mechanics and Control, Russian Academy of Sciences, 24 Rabochaya Str., Saratov 410028, Russia

*** e-mail:** versetty2005@yandex.ru

Abstract. The kinetics of collimated transmittance of the gastric mucosa under the action of an aqueous 40%-glucose solution was experimentally investigated. Based on the analysis of the transmittance kinetics, the value of the effective diffusion coefficient of glucose in the gastric mucosa was estimated and amounted to $(1.59\pm0.96)\times10^{-6}$ cm^2/s. The permeability coefficient of the mucosa for glucose, calculated using the first Fick diffusion law, was estimated as $(2.81\pm0.90)\times10^{-5}$ cm/s. It was shown that the introduction of the glucose solution into the mucosa reduced the light scattering coefficient by approximately 5–10%. The increase in the depth of light penetration was from 5% to 15%, depending on the selected spectral range. The results can be used to develop new methods of diagnosis and treatment of stomach diseases. © 2019 Journal of Biomedical Photonics & Engineering.

Keywords: glucose; diffusion coefficient; permeability coefficient; light penetration depth; gastric mucosa; optical clearing.

Paper #3327 received 16 Jul 2019; revised manuscript received 14 Sep 2019; accepted for publication 21 Sep 2019; published online 30 Sep 2019. doi: 10.18287/JBPE19.05.030302.

1 Introduction

Currently, non-invasive optical methods for diagnostics and therapy of various diseases are widely used in medicine, due to their safety for the health of patients and low cost [1–7]. At the same time, one of the main problems in their application is related to the delivery of probe radiation through the surface of biological tissue to the required depth. The complexity of this problem solving is associated with the limitations imposed by the scattering ability of biological tissues, which is the cause of the decrease in spatial resolution and depth of probing in the visible and near-infrared (NIR) spectral ranges [3]. It is well known that the optical radiation scattering in tissues is mainly connected with the mismatch of refractive indices of the tissue structural components (e.g. collagen and elastin fibers) and the interstitial fluid, as well as between cellular organelles and cytoplasm [3]. As shown in numerous studies (see, for example, Refs. [8–15]), the scattering properties of biological tissues can be effectively controlled by action of hyperosmotic immersion optical clearing agents (OCAs), which cause diffusion of water from interstitial space and partially replace the interstitial fluid. This method is known in literature as a “tissue optical clearing” technique. The introduction of an OCA with a higher refractive index than an interstitial fluid into tissue leads to matching the refractive indices of the scatterers and the interstitial fluid, which significantly reduces light scattering in the biological tissue. The described method of the control of tissue optical characteristics is important both for studying fundamental laws of tissue metabolism and for development of the optical and laser methods of diagnostics, therapy and surgery.

Among substances used as OCAs, a special place is occupied by aqueous solutions of glucose of various concentrations due to their biocompatibility and low cost [8–20]. Most often, glucose solutions are used for the optical clearing of connective tissues, such as skin dermis, sclera, *dura mater*, etc. In addition, the optical clearing of blood in the presence of glucose contributes to development of methods for blood glucose monitoring [11, 12, 20, 21].

At the same time, despite such numerous studies, the optical clearing of gastrointestinal tract mucosa has been studied not enough. It has been shown that the use of OCAs, such as glycerol and dimethyl sulfoxide (DMSO) solutions, contributes to effective optical clearing of the stomach tissues in the NIR spectral region [22–25]. At this the use of aqueous glucose solutions is not sufficiently studied, although some investigations have suggested differentiation of normal and tumor tissues of the stomach, colon and esophagus based on the difference in their permeability to aqueous solutions of glucose [16, 26–28]. It should be noted that despite a number of works aimed at measuring the tissue permeability coefficients for aqueous glucose solutions [16, 26–28], we could not find a single work devoted to the measuring of the glucose diffusion coefficient in the gastric mucosa.

It is obvious that the knowledge of the diffusion coefficients of OCAs in biological tissues is necessary for the development and optimization of tissue optical clearing technique. Therefore, the purpose of this work is to study the temporal dependence of collimated transmittance of the gastric mucosa under the action of the aqueous 40%-glucose solution and evaluate on this basis the effectiveness of tissue optical clearing as well as the glucose diffusion coefficient in the mucosa.

2 Materials and Methods

The study was performed with 10 samples of the human gastric mucosa, from different patients obtained in the course of planned operations or anatomical investigations. The experimental studies were approved by the Ethics Committee of V.I. Razumovsky Saratov State Medical University. Immediately after autopsy, tissue samples were placed in a 0.9% NaCl solution and were kept in it until spectral measurements for 4–8 h at ~4°C. The area of the samples was approximately 1.5×1 cm^2, the average thickness measured with an electronic micrometer varied from 0.36±0.10 to 0.70±0.20 mm.

The spectra of collimated transmittance of the gastric mucosa were measured using a multichannel USB4000-Vis-NIR spectrometer (Ocean Optics, USA) in the spectral range of 400–1000 nm. The tissue sample was fixed on a plastic plate (size 3.5×1.5 cm^2) with a rectangular hole in the center (size 8×8 mm^2) and placed in a 5 mL glass cuvette with glucose solution. The cuvette was placed between two QP400-1-VIS-NIR optical fibers (Ocean Optics, USA) with 400 μm core diameter. To provide the beam collimation, the collimators 74-ACR (Ocean Optics, USA) were fixed at the ends of the fibers, using standard SMA-905 connectors. Halogen lamp HL-2000 (Ocean Optics, USA) was used as a light source. The spectra of collimated transmittance were recorded every 1–2 min for 30 min after placing the mucosa sample into glucose solution. The measurement error did not exceed 5% of the measured value in the wavelength range above 500 nm and 10% in the shorter wavelength region of the spectrum. The measurement error (the standard deviation) included collimation error, instrumental error, light source fluctuations, etc., and tissue optical properties variability. For assessment of the error, the collimated transmittance spectrum of the thickest tissue sample (with thickness of 0.70±0.20 mm) was measured in empty cuvette, without optical clearing agent, ten times. At that the tissue sample was taken out and put into cuvette again to take into account the variability of the tissue optical properties in different part of the sample. After that the mean and the standard deviation were calculated for each wavelength. All measurements were carried out at room temperature ~20°C.

Commercially available aqueous 40%-glucose solution for injection (Dalchempharm, Russia) was used as an OCA. The pH of this solution was measured using pH-meter (Hanna, Germany) as 3.5. The refractive index of the solution was measured with a multiwavelength refractometer Abbe DR-M2/1550 (ATAGO, Japan) at 12 wavelengths in the spectral range of 480–1550 nm with precision of 0.0002 and the measurement results are presented in Table 1.

Interpolation was performed using the Sellmeier dispersion formula [29], presented in the form:

$$n(\lambda)=\sqrt{\frac{2P(\lambda)+1}{1-P(\lambda)}}, \qquad (1)$$

where $P(\lambda)=a_0+a_1\lambda^{*2}+\frac{a_2}{\lambda^{*2}}+\frac{a_3}{\lambda^{*2}-\lambda_{UV}^2}+\frac{a_4}{\lambda^{*2}-\lambda_{IR}^2}$;

n is the refractive index of an aqueous solution of glucose; $\lambda^*=\lambda/\lambda_0$ is the relative wavelength, λ_0 = 589 nm; λ_{UV} = 229.202 nm; λ_{IR} = 5432.937 nm; λ is the wavelength in nm. The interpolation coefficients (a_0, a_1, a_2, a_3, a_4) are shown in Table 2.

In the study of the interaction between the glucose solution and samples of the mucosa, it was assumed that only the refractive index of the interstitial fluid is changed due to glucose diffusion into the sample and osmotic outflow of water from the tissue. In this case, the refractive indices of the scatterers and the interstitial fluid were matched, which led to a decrease in the scattering coefficient of the tissue. The study of the kinetics of this process allows for estimation of the diffusion coefficient as a measure of the mean exchange flow rate of glucose molecules into the tissue [30]. This means that for the treatments of mucosa with 40%-glucose solution, in particular, glucose diffuses into the

Table 1 The refractive indices of the aqueous 40%-glucose solution, measured at different wavelengths

λ, nm	480	486	546	589	644	656	680	800	930	1100	1300	1550
n	1.3957	1.3959	1.3925	1.391	1.3891	1.3886	1.3877	1.3846	1.3813	1.378	1.3748	1.371

Table 2 The interpolation coefficients of the spectral dependence of the refractive index of the aqueous 40%-glucose solution

a_0	a_1	a_2	a_3	a_4
0.27094	-1.0746×10^{-3}	5.34504×10^{-3}	991.71185	5.5939×10^{5}

tissues during all the treatment due to equilibrium between the water in the immersing solution and the water inside the tissue. The water flow is insignificant and the coefficients of permeability and diffusion are determined only by the slower diffusion of glucose molecules [28].

The process of glucose transport in the gastric mucosa was described in the framework of the free diffusion model. The following assumptions were made regarding the transfer process: 1) only concentration diffusion takes place, i.e. the exchange flux of glucose into biological tissue and water from the tissue at this point is proportional to the gradient of glucose concentration at this point; 2) the diffusion coefficient is constant at all points inside the sample of biological tissue. The solution of the diffusion equation, described in detail in Ref. [30], made it possible to estimate the average concentration of glucose solution inside the sample at each time point.

In the first approximation, solution of the second Fick diffusion law equation has the form [30]:

$$C(t) = C_0\left(1-\exp\left(-\frac{t}{\tau}\right)\right), \qquad (2)$$

where $C(t)$ is the volume-averaged concentration of OCA inside the sample; C_0 is the concentration of glucose in the immersion solution; t is the time, sec; $\tau = \frac{l^2}{\pi^2 D}$ is the characteristic diffusion time, sec; l is the thickness of the sample of mucosa, cm; D is the diffusion coefficient, cm^2/s.

As it was shown earlier [17, 28, 31–34], the dependence of the collimated transmittance T_c of a tissue sample placed in an immersion liquid, over time, for each wavelength, can be represented as:

$$T_c(t) \approx \frac{C(t)}{C_0} = 1-\exp\left(-\frac{t}{\tau}\right). \qquad (3)$$

Measurement of the characteristic diffusion time τ was carried out using the least squares method:

$$\tau = -\frac{\sum_{j=1}^{N} t_j^2}{\sum_{j=1}^{N}\left(t_j \ln y_j\right)},$$

where t_j is the moment of measurement of each value T_c, $y = 1-T_c/A$; A is the maximum value of the collimated transmittance, N is the total number of experimental points obtained by registering the kinetics of collimated transmittance at a fixed wavelength. Accordingly, the diffusion coefficient D was determined from the relationship:

$$D = \frac{l^2}{\pi^2 \tau}. \qquad (4)$$

After determining of the value of D from the analysis of the collimated transmittance kinetics, measured at each individual wavelength, the obtained values were averaged over all wavelengths of the measured spectral range.

Knowledge of the value of D allowed us to determine the permeability coefficient (P) of the biological tissue under study for a diffusing substance, associated with the value of the diffusion coefficient by the expression [35]:

$$P = \frac{D}{l}. \qquad (5)$$

The optical clearing efficiency (OCE) is one of the most important parameters, allowing to evaluate the effectiveness of the use of those or other clearing agents and to compare them with each other. Quantitatively, the efficiency of optical clearing is determined by the expression [17, 31, 36–38]:

$$\mathrm{OCE} = \frac{\mu_t(t=0) - \mu_t^{\min}}{\mu_t(t=0)}, \qquad (6)$$

where $\mu_t = -\ln(T_c)/l$ is the attenuation coefficient, 1/cm; $\mu_t^{\min}$ is the minimal value of the attenuation

coefficient measured during the optical clearing process, 1/cm. In the framework of this work, the OCE values were determined for each wavelength in each of the three selected spectral ranges (500–600 nm, 600–700 nm and 700–900 nm), and then the obtained values were averaged.

Another important characteristic for correct determination of the radiation dose in the course of photochemical and photodynamic therapy of various diseases, as well as the dosimetry of optical radiation at laser surgery of a stomach ulcer is the depth of light penetration. In diffusion approximation, the assessment of the depth of light penetration into biological tissue (δ) is performed using the expression: $\delta = 1/\sqrt{3\mu_a(\mu_a + \mu_s')}$ [1]. This expression is true when a "pencil" beam is incident on the surface of the scattering medium, and the diffuse radiant fluence mainly is created by diffusely scattered photons. We have previously shown [39] that the maximum effect is observed in the spectral region of 700–900 nm, where the depth of light penetration approximately corresponds to the total thickness of the gastric mucosa/submucosa and muscle layer and amounts more than 3 mm, which indicates a sufficiently large amount of radiation penetrating into the abdominal cavity. In the spectral range above 900 nm with increasing wavelength, the depth of light penetration significantly decreases to 0.6 mm in the region of the water absorption band with a maximum on 1940 nm. Analysis of the penetration depth of ballistic photons used for imaging in OCT or confocal microscopy can be performed on the basis of the expression [40]:

$$\delta_c = 1/\mu_t . \qquad (7)$$

The values δ_c were determined for each wavelength in each of the three selected spectral ranges (500–600 nm, 600–700 nm, and 700–900 nm), and then the resulting values were averaged. The change in the depth of penetration of ballistic photons was estimated using the expression:

$$\Delta\delta_c = \frac{\delta_c^{\max} - \delta_c(t=0)}{\delta_c(t=0)} . \qquad (8)$$

Here $\delta_c^{\max}$ is the maximal value of the light penetration depth measured during the optical clearing process, 1/cm.

3 Results and Discussion

Figs. 1 and 2 present the typical spectral and temporal dependences of the collimated transmittance of the sample of gastric mucosa affected by the studied glucose solution. Fig. 1 shows that at the initial moment the sample of mucosa is not transparent to optical radiation. In the process of replacing water molecules in the interstitial fluid with glucose molecules, we have observed the increase in optical transmittance, i.e., the mucosa transparency, which is due to the matching of refractive indices of the interstitial fluid and the tissue scatterers. As a result, the scattering has been reduced and the collimated transmittance has been increased.

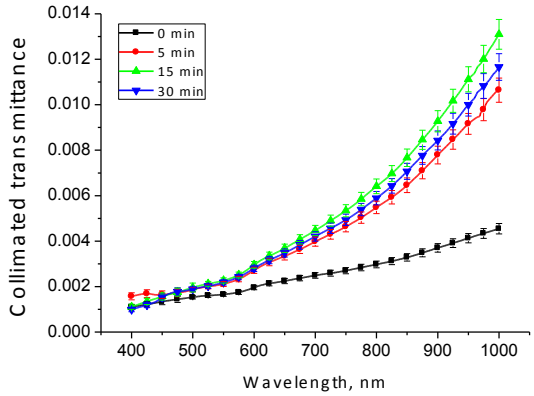

Fig. 1 Typical collimated transmittance spectra of gastric mucosa influenced by aqueous 40%-glucose solution measured in different time intervals.

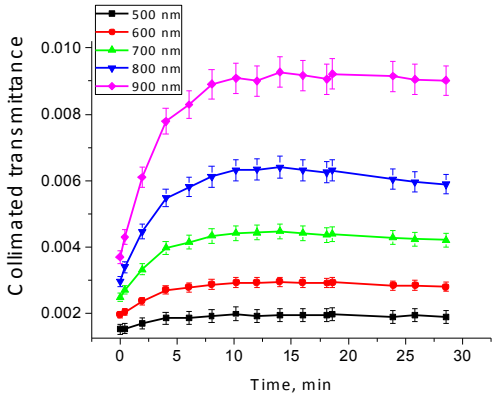

Fig. 2 Typical collimated transmittance kinetics of the gastric mucosa influenced by aqueous 40%-glucose solution measured for different wavelengths.

From Fig. 2, it follows that the maximum clearing effect of the gastric mucosa under the action of the glucose solution is observed in the first 10 min after beginning the experiment, with the greatest effect being achieved in the NIR spectral range, where the collimated transmittance increases by about 2–2.5 fold.

The analysis of the kinetics of collimated transmittance of the gastric mucosa samples with the above presented algorithm was used for estimation of the relative diffusion coefficient of 40%-glucose solution in the tissue; and the value amounted to $(1.59\pm0.96)\times10^{-6}$ cm^2/s. The corresponding value of permeability coefficient was estimated as $(2.81\pm0.90)\times10^{-5}$ cm/s. The obtained values agree quite well with the data measured in the works [16, 26–28] and presented in Table 3. From the table, it follows that

Table 3 The permeability coefficients (P), diffusion coefficients (D) and characteristic diffusion time (τ) of aqueous solutions of glucose in mucosa of digestive tract organs

Tissue	Concentration of glucose	P, cm/s	D, cm²/s	τ, s
Mice stomach (l = 330 μm)	20%	(9.4±0.4)×10^{-6} [16]	(3.1±0.1)×10^{-7} *	817.6±26.4 **
Normal human colon (l = 391 μm)	30%	(3.37±0.23)×10^{-6} [26]	(1.318±0.090)×10^{-7} *	1928.0±132.1 **
Human normal esophagus (l = 500 μm)	40%	(1.74±0.04)×10^{-5} [27]	(8.7±0.2)×10^{-7} *	291.3±6.7 **
Healthy colorectal mucosa (l = 500 μm)	20%	(7.782±0.024)×10^{-5} ***	(3.891±0.012)×10^{-6} ****	65.1±0.2 [28]
Healthy colorectal mucosa (l = 500 μm)	25%	(7.31±0.34)×10^{-5} ***	(3.655±0.169)×10^{-6} ****	69.4±3.2 [28]
Healthy colorectal mucosa (l = 500 μm)	30%	(6.27±0.47)×10^{-5} ***	(3.135±0.236)×10^{-6} ****	81.1±6.1 [28]
Healthy colorectal mucosa (l = 500 μm)	35%	(3.66±0.16)×10^{-5} ***	(1.83±0.08)×10^{-6} ****	138.4±5.9 [28]
Healthy colorectal mucosa (l = 500 μm)	40%	(1.693±0.027)×10^{-5} ***	(8.467±0.133)×10^{-7}****	299.2±4.7 [28]
Healthy colorectal mucosa (l = 500 μm)	45%	(2.396±0.069)×10^{-5} ***	(1.198±0.035)×10^{-6} ****	211.5±6.1 [28]
Healthy colorectal mucosa (l = 500 μm)	50%	(4.858±0.061)×10^{-5} ***	(2.43±0.03)×10^{-6} ****	104.3±1.3 [28]
Human gastric mucosa (l = 530±240 μm)	40%	(2.81±0.90)×10^{-5} [This work]	(1.59±0.96)×10^{-6} [This work]	191.40±0.34 [This work] 219.2±159.0 **

* the diffusion coefficient calculation was performed using the expression $D = Pl$.

** the characteristic diffusion time calculation was performed using the expression $\tau = \frac{l^2}{\pi^2 D}$ for sample thickness 500 μm.

*** the permeability coefficient calculation was performed using the expression (5).

**** the diffusion coefficient calculation was performed using the expression $D = \frac{l^2}{\pi^2 \tau}$.

literature data for glucose diffusion coefficients in the digestive tract mucosa are in the range from (1.318±0.090)×10^{-7} cm^2/s [26] to (3.891±0.012)×10^{-6} cm^2/s [28]. Thus, the value obtained in this paper for glucose diffusion coefficient is in the range of values obtained by other researchers. The differences could be originated from different concentration of glucose solution used in the measurements, because, as it was shown in Refs. [28, 32–34], measured values significantly depend on glucose concentration, and also on pH. Similarly, the permeability coefficient measured in this paper is also in the range of published data (3.37±0.23)×10^{-6} cm/s [26] and (7.782±0.024)×10^{-5} cm/s [28].

Unfortunately, a direct comparison of the obtained values of the mass transport parameters (coefficients of diffusion and permeability) is rather difficult, due to the use of different measurement and experimental data processing methods, as well as different structural and morphological features of the studied tissues. So, for example, the authors of [16, 26, 27] used optical coherence tomography signal slope analysis (OCTSS) [13] for measuring the permeability coefficient of the mucosa. The authors of Ref. [28] performed the measurement of glucose diffusion rate using transmission spectroscopy (like the authors of the presented work), but the results were presented in the form of characteristic diffusion times of glucose. To compare our data and data obtained by other researchers, we recalculated the values of permeability coefficients or characteristic diffusion times that they obtained, into the values of diffusion coefficients. The results are presented in Table 3.

Table 4 The efficiency of optical clearing (OCE), calculated using Eq. (6) and the depth of penetration of collimated radiation, calculated using Eqs. (7) and (8)

	Spectral range		
	500-600 nm	600-700 nm	700-900 nm
OCE	(500.0±2.5)×10^{-4}	(810.0±3.6)×10^{-4}	(1310±4)×10^{-4}
$\delta_c(t=0)$, μm	83.0±0.8	86.9±0.9	91.2±1.8
$\delta_c^{\max}$ $(t \approx 20\,\text{min})$, μm	87.4±1.6	94.5±1.9	104.8±4.4
$\Delta\delta_c$	0.053±0.019	0.088±0.021	0.149±0.046

The results of measurements of the efficiency of optical clearing and the change in the depth of collimated radiation penetration in the three spectral ranges are presented in Table 4. It is clearly seen that an aqueous solution of glucose significantly reduces light scattering in the gastric mucosa, thereby increases the penetration depth of probe radiation, which is crucial for planning and conducting diagnostic or therapeutic procedures, including laser surgery of a stomach ulcer.

To comparison the OCE of the investigated 40%-glucose solution with other optical clearing agents (such as glycerol and DMSO solutions) we calculated relative increasing of stomach tissue transmittance as $\Delta T = \frac{T(t=30\,\text{min}) - T(t=0\,\text{min})}{T(t=0\,\text{min})} \times 100\%$ [25] in the spectral range 800-1000 nm. In our experiments we obtained the $\Delta T \approx 26.3 \pm 0.14\%$. In the work [22] it was found that light transmittance was increased by approximately 23% at 30 min after 80%-glycerol solution, while 15% and 11% were obtained after the treatment of the tissue with 50%-glycerol and 50%-DMSO, respectively. It should be noted that the use of mixure of 50%-glycerol solution with 30%-DMSO solution for optical clearing increases the transmittance up to approximately 29% at 30 min after the application [25]. Thus, we can see that OCE of 40%-glucose solution is comparable with OCE of glycerol and DMSO solutions used for stomach tissue optical clearing.

3 Conclusion

The paper presents results of measurement of the diffusion coefficient of glucose in the gastric mucosa *in vitro*. The measured value of the relative diffusion coefficient is $(1.59\pm0.96)\times10^{-6}$ cm^2/s, which allows estimating the value of the mucosal permeability coefficient for glucose molecules as $(2.81\pm0.90)\times10^{-5}$ cm/s. It is shown that the administration of an aqueous solution of glucose into the mucosa provides a decrease in the light scattering coefficient by approximately 5–10%. The increase in the light penetration depth is from 5% to 15%, depending on the selected spectral range.

The results obtained has allowed us to evaluate the effectiveness of using the aqueous 40%-glucose solution as an optical clearing agent for controlling the optical characteristics of the gastric mucosa, and they can be used to develop new methods for diagnostics and treatment of stomach diseases.

Disclosures

All authors declare that there is no conflict of interests in this paper.

Acknowledgement

The study was supported by the RFBR grant No. 19-32-90224.

References

1. V. V. Tuchin, Tissue Optics: Light Scattering Methods and Instruments for Medical Diagnosis, 3rd Edition, SPIE Press, Bellingham, Washington (2015).
2. V. V. Tuchin (Ed.), Handbook of Optical Biomedical Diagnostics, 2nd Edition, SPIE Press, Bellingham, Washington (2016).
3. V. V. Tuchin, "Tissue optics and photonics: light-tissue interaction," Journal of Biomedical Photonics & Engineering 1(2), 98–134 (2015).
4. A. J. Welch, M. J. C. van Gemert (Eds.), Optical-thermal response of laser-irradiated tissue, 2nd Edition, Springer (2011).
5. D. A. Boas, C. Pitris, and N. Ramanujan (Eds.), Handbook of Biomedical Optics, CRC Press, Taylor & Francis Group (2011).
6. S. H. Yun, S. J. J. Kwok, "Light in diagnosis, therapy and surgery," Nature Biomedical Engineering 1(1), 0008 (2017).
7. A. Méndez, "Optics in Medicine," Chap. 13 in Optics in Our Time, M. Al-Amri, M. El-Gomati, and M. Zubairy (Eds.), Springer, 299–333 (2016).
8. I. Carneiro, S. Carvalho, V. Silva, R. Henrique, R. Oliveira, and V. V. Tuchin, "Kinetics of optical properties of human colorectal tissues during optical clearing: a comparative study between normal and pathological tissues," Journal of Biomedical Optics 23(12), 121620 (2018).
9. W. Feng, R. Shi, N. Ma, D. K. Tuchina, V. V. Tuchin, and D. Zhu, "Skin optical clearing potential of disaccharides," Journal of Biomedical Optics 21(8), 081207 (2016).
10. E. A. Genina, A. N. Bashkatov, and V. V. Tuchin, "Glucose-induced optical clearing effects in tissues and blood," Chap. 21 in Handbook of Optical Sensing of Glucose in Biological Fluids and Tissues, V. V. Tuchin (Ed.), Taylor & Francis Group LLC, CRC Press, 657–692 (2009).
11. E. A. Genina, A. N. Bashkatov, and V. V. Tuchin, "Tissue optical immersion clearing," Expert Review of Medical Devices 7(6), 825–842 (2010).

12. E. A. Genina, A. N. Bashkatov, Yu. P. Sinichkin, I. Yu. Yanina, and V. V. Tuchin, "Optical clearing of tissues: benefits for biology, medical diagnostics, and phototherapy," Chap. 10 in Handbook of Optical Biomedical Diagnostics, 2nd Edition, V. V. Tuchin (Ed.), SPIE Press, Bellingham, Washington, 565–637 (2016).
13. K. V. Larin, M. G. Ghosn, A. N. Bashkatov, E. A. Genina, N. A. Trunina, and V. V. Tuchin, "Optical clearing for OCT image enhancement and in-depth monitoring of molecular diffusion," IEEE Journal of Selected Topics in Quantum Electronics 18(3), 1244–1259 (2012).
14. J. Wang, N. Ma, R. Shi, Y. Zhang, T. Yu, and D. Zhu, "Sugar-induced skin optical clearing: from molecular dynamics simulation to experimental demonstration," IEEE Journal of Selected Topics in Quantum Electronics 20(2), 7101007 (2014).
15. D. Zhu, K. Larin, Q. Luo, and V. V. Tuchin, "Recent progress in tissue optical clearing," Laser & Photonics Reviews 7(5), 732–757 (2013).
16. H. Xiong, Z. Guo, C. Zeng, L. Wang, Y. He, and S. Liu, "Application of hyperosmotic agent to determine gastric cancer with optical coherence tomography *ex vivo* in mice," Journal of Biomedical Optics 14(2), 024029 (2009).
17. D. K. Tuchina, R. Shi, A. N. Bashkatov, E. A. Genina, D. Zhu, Q. Luo, and V. V. Tuchin, "Ex vivo optical measurements of glucose diffusion kinetics in native and diabetic mouse skin," Journal of Biophotonics 8(4), 332–346 (2015).
18. D. K. Tuchina, P. A. Timoshina, V. V. Tuchin, A. N. Bashkatov, and E. A. Genina, "Kinetics of rat skin optical clearing at topical application of 40% glucose: *ex vivo* and *in vivo* studies," IEEE Journal of Selected Topics in Quantum Electronics 25(1), 7200508 (2019).
19. D. K. Tuchina, A. N. Bashkatov, E. A. Genina, and V. V. Tuchin, "Quantification of glucose and glycerol diffusion in myocardium," Journal of Innovative Optical Health Sciences 8(3), 1541006 (2015).
20. H. Ullah, F. Hussain, and M. Ikram, "Optical coherence tomography for glucose monitoring in blood," Applied Physics B 120, 355–366 (2015).
21. R. V. Kuranov, V. V. Sapozhnikova, D. S. Prough, I. Cicenaite, and R. O. Esenaliev, "*In vivo* study of glucose-induced changes in skin properties assessed with optical coherence tomography," Physics in Medicine & Biology 51, 3885–3900 (2006).
22. R. K. Wang, X. Xu, Y. He, and J. B. Elder, "Investigation of optical clearing of gastric tissue immersed with hyperosmotic agents," IEEE Journal of Selected Topics in Quantum Electronics 9(2), 234–242 (2003).
23. X. Xu, R. Wang, and J. B. Elder, "Optical clearing effect on gastric tissues immersed with biocompatible chemical agents investigated by near infrared reflectance spectroscopy," Journal of Physics D: Applied Physics 36, 1707–1713 (2003).
24. Y. He, R. K. Wang, "Dynamic optical clearing effect of tissue impregnated with hyperosmotic agents and studied with optical coherence tomography," Journal of Biomedical Optics 9(1), 200–206 (2004).
25. X. Xu, R. K. Wang, "Synergistic effect of hyperosmotic agents of dimethyl sulfoxide and glycerol on optical clearing of gastric tissue studied with near infrared spectroscopy," Physics in Medicine and Biology 49, 457–468 (2004).
26. Q. Zhao, C. Zhou, H. Wei, Y. He, X. Chai, and Q. Ren, "*Ex vivo* determination of glucose permeability and optical attenuation coefficient in normal and adenomatous human colon tissues using spectral domain optical coherence tomography," Journal of Biomedical Optics 17(10), 105004 (2012).
27. Q. L. Zhao, J. L. Si, Z. Y. Guo, H. J. Wei, H. Q. Yang, G. Y. Wu, S. S. Xie, X. Y. Li, X. Guo, H. Q. Zhong, and L. Q. Li, "Quantifying glucose permeability and enhanced light penetration in *ex vivo* human normal and cancerous esophagus tissues with optical coherence tomography," Laser Physics Letters 8(1), 71–77 (2011).
28. S. Carvalho, N. Gueiral, E. Nogueira, R. Henrique, L. Oliveira, and V. V. Tuchin, "Glucose diffusion in colorectal mucosa - a comparative study between normal and cancer tissues," Journal of Biomedical Optics 22(9), 091506 (2017).
29. P. Schiebener, J. Straub, J. M. H. L. Sengers, and J. S. Gallagher, "Refractive index of water and steam as function of wavelength, temperature and density," Journal of Physical and Chemical Reference Data 19(3), 677–717 (1990).
30. A. N. Bashkatov, E. A. Genina, and V. V. Tuchin, "Measurement of glucose diffusion coefficients in human tissues," Chap. 19 in Handbook of Optical Sensing of Glucose in Biological Fluids and Tissues, V. V. Tuchin (Ed.), Taylor & Francis Group LLC, CRC Press, 587–621 (2009).
31. V. D. Genin, D. K. Tuchina, A. J. Sadeq, E. A. Genina, V. V. Tuchin, and A. N. Bashkatov, "*Ex vivo* investigation of glycerol diffusion in skin tissue," Journal of Biomedical Photonics & Engineering 2(1), 010303 (2016).
32. L. M. Oliveira, M. I. Carvalho, E. Nogueira, and V. V. Tuchin, "The characteristic time of glucose diffusion measured for muscle tissue at optical clearing," Laser Physics 23(7), 075606 (2013).
33. L. Oliveira, M. I. Carvalho, E. M. Nogueira, and V. V. Tuchin, "Diffusion characteristics of ethylene glycol in skeletal muscle," Journal of Biomedical Optics 20(5), 051019 (2015).
34. I. Carneiro, S. Carvalho, R. Henrique, R. M. Oliveira, and V. V. Tuchin, "A robust *ex vivo* method to evaluate the diffusion properties of agents in biological tissues," Journal of Biophotonics 12(4), e201800333 (2019).
35. A. Kotyk, K. Janacek, Membrane Transport: An Interdisciplinary Approach, Plenum Press, New York (1977).

36. D. Zhu, J. Wang, Z. Zhi, X. Wen, and Q. Luo, "Imaging dermal blood flow through the intact rat skin with an optical clearing method," Journal of Biomedical Optics 15, 026008 (2010).
37. B. Choi, L. Tsu, E. Chen, T. S. Ishak, S. M. Iskandar, S. Chess, and J. S. Nelson, "Determination of chemical agent optical clearing potential using in vitro human skin," Lasers in Surgery and Medicine 36, 72–75 (2005).
38. D. K. Tuchina, V. D. Genin, A. N. Bashkatov, E. A. Genina, and V. V. Tuchin, "Optical clearing of skin tissue ex vivo with polyethylene glycol," Optics and Spectroscopy 120(1), 28–37 (2016).
39. A. N. Bashkatov, E. A. Genina, V. A. Grishaev, S. V. Kapralov, V. I. Kochubey, and V. V. Tuchin, **"**Study of the changes of gastric wall mucosa optical properties under the impact of aqueous solutions of haemoglobin and glucose for improving conditions of the laser coagulation," Journal of Biomedical Photonics & Engineering 3(4), 040304 (2017).
40. S. Golovynskyi, I. Golovynska, L. I. Stepanova, O. I. Datsenko, L. Liu, J. Qu, and T. Y. Ohulchanskyy, "Optical windows for head tissues in near-infrared and short-wave infrared regions: approaching transcranial light applications," Journal of Biophotonics 11(12), e201800141 (2018).

Modelling Of PAFC Based Scattering Monitoring System for the Characterization of the Therapeutic Micro-Bubbles

Vibhor K. Bhardwaj* **and Surita Maini**
Department of Electrical and Instrumentation Engineering, Sant Longowal Institute of Engineering & Technology, Punjab 148106, India

*** e-mail:** vibhorkrbhardwaj@gmail.com

Abstract. In recent years, researchers are eagerly developing the Ultrasound Cavity Agents (UCA) as a therapeutic agent, so that they can deliver the drugs to an intended place in a guided manner with minimal invasiveness and maximum effectiveness. However, control dissolution of the drug is still an issue because the shell of the micro-bubble sometimes collapses instantaneously and start releasing the drug at a faster rate. This sudden rise in the pressure's level can rupture the capillaries and sometimes blood vessels also. Therefore, in such cases, it is a great challenge to examine the dynamics of the micro-bubble as well as the health of the blood vessel. In this essence, this paper presents a study based on the finite element method to examine the potential use of Photo-Acoustic Flow Cyclometery (PAFC) to resolve this issue. The presented model is based on the study of the intensity variations of the optical scatterings engender by the micro-bubbles through PAFC. The results of the study reveal that the proposed model has the potential to be used as a new mechanism to examine the growth of the micro-bubble as well as the health of the blood vessel. Moreover, by analysing the scattering pattern, one can also able to predict the value of the cavitation threshold and the size of the micro-bubble. Hence, the authors envisioned that the modified PAFC system can lead the path of a low-cost and real-time examiner for accurate target drug delivery as well as for the health of the blood vessel. Which in turn potentially increases the localized concentration of the drug to reduce the concerned side-effects of medicine on the other part of the body.

Keywords: therapeutic agents; microbubble; PAFC; FEM; cavitation threshold.

Paper #3335 received 6 Aug 2019; revised manuscript received 26 Sep 2019; accepted for publication 26 Sep 2019; published online 30 Sep 2019. doi: 10.18287/JBPE19.05.030303.

1 Introduction

In the present decade, the advances of biomedical science have focused the research in the new minimal-invasive method for targeted drug delivery. Compare to conventional therapies this method provides a strict localization of the drugs at the vascular pathology sites. Therefore, a significant improvement has been observed in therapeutic efficacy without any drug toxicity and systematic side-effects. In recent years, researchers are eagerly discovering the potential use of ultrasound contrast agents (UCAs) as a transporter to deliver the drug at a specific location. Due to their small size (mean diameter of 1.1 to 3.3 μm), they can easily travel into small peripheral capillaries of blood along with blood-stream [1–3]. In contrast to its primary role as a diagnostic tool to improve imaging modality of the small vessels of the human organs, they have potential to be used as a therapeutic agent having drugs in their core [4]. These therapeutic agents have potential application in the treatment of a certain type of cancer, thrombolysis [5–7], real-time and non-invasive blood pressure measurement [8] during surgery and many more.

Till now various studies have been conducted to understand the interaction of bubble with a blood vessel,

determination of the size of the bubbles, the evolution of the bubble size, effect of resonance on the bubble, and discrimination of bubbles with other particles, etc. [9–12]. But still, there are many challenges, which must be addressed before making it a tested and trusted tool. Moreover, their further therapeutic capabilities are still being explored by several research groups in different countries, but the results are not yet concluded.

These challenges, however, propelling the researchers towards a new field of bubble dynamics to understand the therapeutic capability of the micro-bubble for different ailments in the different organs. Furthermore, the behaviour and characterization of the bubbles are also an important aspect for the medical imaging, therapy, and diagnostic field.

Commonly, the characterization of the microbubble is conducted by the mean of measuring the acoustic scattering and attenuations. However, this method is unable to characterize the free micro-bubbles due to the limitation of acoustic resolution and the bandwidth of the acoustic receivers [13, 14]. Therefore, for the characterization of an individual microbubble, optical imaging techniques have been used consisting of high-speed cameras and streak cameras. But, this technique produces a huge amount of processed data, thus limiting its operation only for few-cycle of ultrasound [15, 16].

To overcome this problem, another alternative approach for characterization is based on the analysis of scattered light [17, 18]. This method not only reduces the amount of data per oscillation cycle but also capable to characterize the dynamics of the whole microbubble population. As compare to high-speed imaging, this method is unable to provide direct visual information about the dynamics of the microbubble. But, low cost and ease of incorporation with ultrasound devices make this method more promising for further research [19].

Considering the above challenges, the authors present a Photo Acoustic Flow Cytometer (PAFC) based model for real-time observation of the micro-bubble dynamics. In this model, the PAFC has been used to create acoustic pressure that expands the micro-bubble shell and thereby providing an intensity variation in the scattered light. Thus, by analysing the scattering pattern, one can also be able to predict the value of the cavitation threshold and the size of the micro-bubble. The study has also presented mathematical modelling along with a finite element modelling of the proposed model. The results of the study reveal that the proposed model has the potential to provide a label-free rapid-assessment of the micro-bubble dynamics to manage adequate intravascular pressure in real time. Moreover, the health of the blood vessel can also be assessed in real time by comparing the reference signal. However, the clinical trials are a more accurate analysis of the system but for examining the feasibility of a novel approach, the computational models have substantial advantages for understanding and translating the outcome.

The system is modelled in COMSOL Multiphysics in the two-dimensional mode. Thus, a realistic finite element representation of the practical problem can be done using coupled physics modelling.

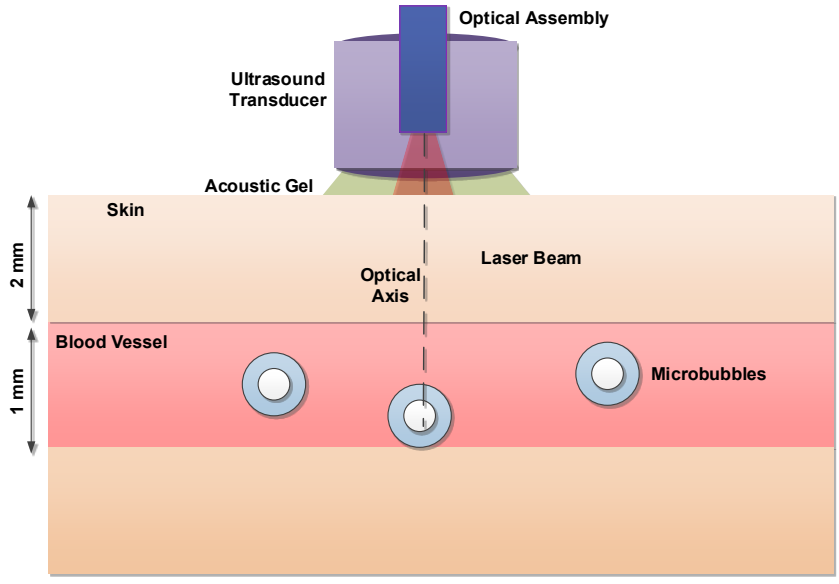

Fig. 1 Illustration of PAFC setup consist of a 4 mm disc-shape ultrasound transducer and a 1024 nm laser beam (fed through a 0.2 mm core multi-mode optical fibre). The numerical aperture (NA) of the transducer assembly is 0.5 to capture wide-angle PA excitation, while the arterial wall has a thickness of 0.2 mm.

2 Method and model description

Conventional flow cytometry (FC) is being used as a popular biological tool for many years [20]. This type of tools is based on the principle of scattering and fluorescent of the laser beam. A more advanced version of FC is a combination of laser and ultrasound techniques and known as photo-acoustic (PA) flow

cytometry (PAFC). This photo-acoustic device enhances the quality of the signal for both the optical and acoustic mechanism. It enhances the laser's sensitivity along with spectral specificity and side by side also improves spatial resolution and depth of penetration for ultrasound [21]. Therefore, by using PAFC a more accurate observation of micro-bubbles size and evolution can be performed, and a more feasible method can be made to manage adequate intravascular pressure for bursting. An illustration of the proposed model is shown in Fig. 1. The ultrasound transducer is used to create acoustic pressure on the micro-bubbles and the laser, and its supporting components are used to examine the real-time behaviour of the micro-bubble. A 1 MHz ultrasound transducer was modelled to detect the laser-induced acoustic waves based on the work of Andrews [22]. While the laser diode was modelled to emit the pulses having 10 ns pulse-width with 10 kHz of reception rate at 1064 nm wavelength. The detail discussion on working principle of PAFC setup is available in several literatures [23, 24]. To ensure the proper bonding between the skin and the ultrasound transducer, typically acoustic gel is used as a conductive medium. However, this acoustic gel absorbed a portion of the emitted laser beam with an absorption coefficient of 0.65 cm^{-1} [25].

2.1 Light scattering and absorption

When light is targeted on a surface, some portion of the light gets extinction due to absorption and scattering. In the case of micro-bubble, this extinction depends on the size of the micro-bubble, thickness of the shell and refractive index of core/shell of the microbubble [26]. Various theories have been developed to explain the scattering of light from the microspheres [27–29]. For example, typical mathematical model for the diffraction of light can be developed using Maxwell's equations in spherical coordinates [30]. However, for ease of understanding, a simple mathematical model is formulated with the assumption that extinction of light in the medium is due to the absorption and scattering only:

$$\sigma_{ext} = \sigma_{abs} + \sigma_{sca}, \quad (1)$$

where $\sigma_{ext}, \sigma_{abs}, \sigma_{sca}$ are the coefficients of extinction, absorption and scattering, respectively. Furthermore, using Mie theory of scattering, if a wave of "λ" wavelength having "I_o" intensity is transmitted through a medium and after transmission "I" intensity wave is received then absorption "A" by the medium can be defined as:

$$A = -log_{10}\left(\frac{I}{I_o}\right). \quad (2)$$

Here, it is also an interesting point that the intensity of scattered light also depends on the angle of observation, extinction coefficient, path length "l" and number density "N" [30–32]:

$$I = I_o e^{-\sigma_{ext} l N}. \quad (3)$$

Thus, contribution in light extinction by the absorption can be expressed as:

$$A = \frac{lN}{2.3}\,\sigma_{ext}. \quad (4)$$

The absorption in the homogenous medium having a concentration of "c" and molar extinction coefficient "ε" can also be defined using Beer-Lambert law as [33]:

$$A = \varepsilon c l. \quad (5)$$

Therefore, from Eqs. (4) and (5), the extinction coefficient can be expressed as:

$$\sigma_{ext} = 2.3\frac{\varepsilon c}{N} \quad (6)$$

2.2 Bubble Discrimination

Globally, there are various commercially available UCA agents which have the potential to be used as a carrier for target drug delivery, like Definity, Optison, Imagify, Sonazoid, Targestar, and MicroMarker. The properties of UCA agents such as shell coating, core-gas, and mean diameters are core parameters, which are required to be studied before implementing in real time situations are listed in Table 1.

Table 1 List of Commercially available ultrasound contrast agents with their manufacture name, coating material and gas filled inside the core.

UCA	Manufacture by	Shell Coating	Core Gas	Mean diameter (μm)
Definity	Lantheus Medical Imaging	Phospho-lipids	C3F8	1.1–3.3
Optison	GE Healthcare	Human albumin	C3F8	3.0–4.5
Imagify*	Acusphere	Polymer	C4F10	1.9–2.2
Sonazoid	Daiichi Pharmaceutical	Lipids	C4F10	2.5–3.0
Targestar	Targeson	Phospho-lipids	C4F10	3.0–4.5
MicroMarker	Bracco	Fatty Acids	C4F10	2.3–2.9

The core of these UCAs, are generally filled with perfluoropropane (C3F8) or perfluorobutane (C4F10) gas and the outer shell is coated to stabilize them so that they can survive long enough in the body without pre-bursting. It is worth to note that long survival time is also a great challenge for microbubbles. Because they are highly compressed compare to blood and tissue layers and their compressibility makes them more scattering element, which is a boon to recognize them. The maximum diameter of these agents has been recorded up to 32 µm but generally, the mean diameter varies between 1.1 to 4.5 µm. However, the selection of the UCA depends on the type of targeted organ and its associated capillary (5 µm), artery (10^3 µm) and arteriole (20 µm) of the human body.

In this paper, Definity has been taken as a reference micro-bubble because of its small and consistently-size with extensive safety experience, which also makes it a prominently used therapeutic agent. Moreover, it is worth to note here that these microbubbles can also be used to measure the amount of blood delivered in a tissue per unit time. In literature, the sub-harmonic oscillations of the microbubble are described by the Church-Hoff equation [34]. This equation describes the behavior of the micro-bubble with the following assumption:

1. There is a zero-surface tension between the micro-bubbles shell and the blood interface.
2. The overall distribution of the microbubbles shell thickness is constant.
3. There is no effect of the driving frequency and acoustic pressure on the behavior of the viscoelastic material used for the micro-bubble formation.

With such assumptions, the linear resonance frequency (f_o) of the micro-bubble for the ultrasound region can be described by:

$$f_o = \frac{\omega_o}{2\pi} = \frac{1}{2\pi R_e}\sqrt{\frac{1}{\rho_B}\left(3kP_o + 12G_s\frac{d_s}{R_e}\right)}. \qquad (7)$$

Moreover, for the incompressible flow of blood, the acoustic pressure (P_s) scattered by the microbubble can be given as [35]:

$$P_s(t) = \rho_B(2v_w^2 + Ra_w), \qquad (8)$$

where R_e is the equilibrium radius of the micro-bubble, ρ_B is the density of blood, k is the poly-tropic exponent, P_o is the atrial blood pressure, G_s is the shear modulus of micro-bubble shell, d_s is the thickness of the microbubble shell, v_w is the wall velocity of micro-bubble, R is the instantaneous radius of the micro-bubble and a_w is the acceleration of micro-bubble wall.

From the above two Eqs. (7) and (8), the conclusion can be drawn that the instantaneous radius of the microbubble under the influence of the ultrasound signal is one of the influencing parameters for both resonance frequency and acoustic pressure used for the bursting.

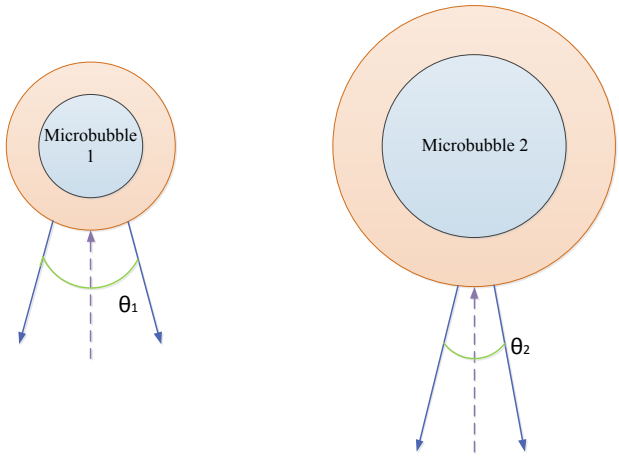

Fig. 2 Indicating the angular distribution of reflected power by two different size microbubbles. The change in the total reflected power occurs due to induction of the different divergence angle (θ). The beam axis has been denoted by a broken line and reflection by a solid line.

Furthermore, the spherical shape of the micro-bubbles produce a partially diffuse reflection (assumed as 0.1 cm^{-1} [36]) thereby scattering intensity follows the exponential relationship with the position of the beam axis [37]. Moreover, as the micro-bubble grows, the curvature of the surface decreases. This subsequently concentrate the laser intensity over a small angle of the divergence angle (θ). Thus, light reflected from a small bubble have less intensity compare to a bubble having higher diameter as illustrated in Fig. 2. Therefore, power distribution of light over the angular range can be used to detect the size or growth of the micro-bubble. Chen et al. [38] modelled the scattering behaviour of the encapsulated microbubble in 2009. The same has been referred in the paper.

3 Boundary Descriptions for Finite Element Analysis

3.1 Boundary Conditions for Microbubble

The model is defined with the following boundary conditions at different interfaces to satisfy the church-Hoff equation is shown in Fig. 3. Furthermore, for a better understanding of dynamics, Marmottant model [39] has been used to characterize the micro-bubble.

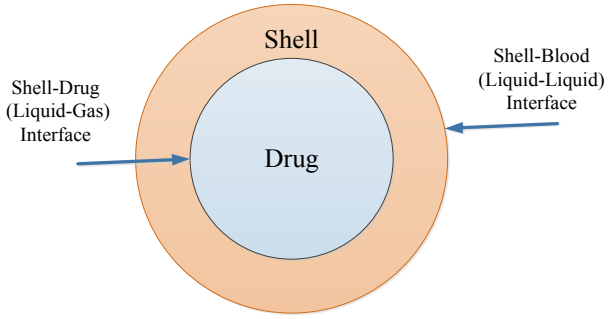

Fig. 3 Illustration of different interfaces of microbubble.

a) Shell-Drug Interface:

Usually, the drug-filled in the micro-bubble is in form of gas [40] and the stabilizing shell is made up of liquids like lipids or proteins and fluorinated gases with a high molecular weight [41]. For this reason, the boundary conditions used for this interface should be followed both the kinematic and dynamic nature of the interface. Therefore, the dynamics conditions have been used to describe the zero-shear stress at the interface while the kinematic condition ensures the stability of the microbubble. Moreover, if the volume of the drug (V_g) inside the micro-bubble remains constant and the gas (drug) satisfying the poly-tropic relation as explained in the equation (7) to determine the linear resonance frequency, then we can define, the relationship between the partial pressure inside the micro-bubble (P_g) and the volume of the (V_g) as

$$P_g V_g^k = constant. \quad (9)$$

b) Shell-Blood Interface:

This interface is defined by dynamic boundary conditions because both the shell and blood are in the liquid state. These dynamic conditions are responsible for providing continuity for both shear stresses and movement of blood and microbubble [42]. Furthermore, interface surface tension, density, perfusion rate, temperature, velocity, pressure, and viscosities of both the medium are also defined by this boundary condition. The parameters used for the modelling are listed in Table 2.

Table 2 Modelling parameter defined for the blood and the artery.

Comput. Domain	Parameter	Value
Artery	Initial Value Modulus	1.74 [MPa]
	Initial Bulk Modulus	34.7 [MPa]
	Young Modulus	6.2 [MPa]
	Density	103 [kg/m^3]
	Poisson's Ratio	0.45
	Model Material	Hyperelastic Neo-Hookean
Blood	Density	1060 [kg/m^3]
	Perfusion Rate	3.6x10^{-3} [1/sec]
	Temperature	37 [°C]
	Viscosity	3.5 [MPa-sec]
	Velocity	1x10-2 [m/sec]
	Pressure	12 [kPa]
	Model Material	Incompressible Navier-Stokes

c) Blood-Skin Interface:

For modelling the blood, a steady flow velocity profile is defined at the inner side of the boundary. The artery is assumed to be non-slip and believed that the blood will not penetrate the wall. Therefore, the velocity of blood flow is uniform and considered to be laminar. The artery parameter like initial shear and bulk modulus, Young modulus, density, Poisson's ratio used for modelling is also listed in Table 2. The absorption coefficient (σ_{abs}) and scattering coefficient (σ_{sca}) of skin used for the modeling are 0.37 and 1 cm^{-1} respectively [43].

3.2 Boundary Conditions for the Rest of the Model

The boundary conditions used for the modeling are depicted in Fig. 4. Because only a section of the human blood vessel has been modelled therefore it becomes necessary to maintain the symmetry of the computational domain to the rest of the domain. So, to make boundaries identical on both the sides of the computational domain Floquet periodic boundary conditions has been applied on both left and right sides of the model. To launch the laser beam, periodic port boundary conditions has been used rather than diffraction order port conditions. Because due roughness of the surfaces, if diffraction order port is used to monitor the reflected and transmitted light, hundreds (or thousands) of diffraction orders are received, which only increases computational complexity. This model is designed only for statistical sampling, hence the relative fraction of laser beam scattered by the microbubble by these different orders has not been considered. Therefore, to compute the reflection and transmission, a perfectly matched layer (PML) is defined above and below of the model and placed at least half a wavelength away to avoid absorption of evanescent field component. Therefore, by using the PMLs we can compute all the unimpeded reflections and avoid using multiple ports to compute total transmittance. Lastly, to evaluate total transmitted and reflected light two additional interior boundaries are placed near the PMLs. These boundaries have been used to integrate the power flux created in both upward and downward directions and are normalized it by the incident power. It is here worth to note that, the acoustic pressure beyond the tolerance of the micro-bubble shell can destruct it instantaneously, and the release of gas with such pressure that can damage adjacent area like blood vessels/capillaries. Thus, it becomes mandatory to apply controlled pressure on the bubble and a systematic incremental in the pressure should be applied with the observation in the bubble growth. The microbubbles considered in this study of the size 1–2, 4–5, 6–8, 8–10 and 10–12 μm are driven at a frequency of 1 MHz with a pressure range of 95 kPa to 333 kPa. In any case, if the pressure increases beyond 333 kPa before target bursting, it may lead to severe complications. The prior bursting reasons may be the different diameter of the bubble, circumstances of the vessel/capillary of the subject, physiochemical properties of blood, different blood pressures, any blockage in a blood vessel and other complications.

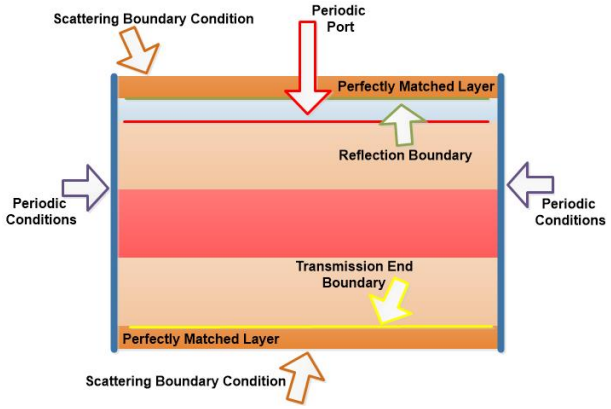

Fig. 4 Boundary conditions for the rest of the model.

4 Results and Discussions

The relative intensity of the light scattered by the microbubble obtained by the proposed model is depicted in Fig. 5 in which an articulate expansion and disruption in the micro-bubble diameter engender by the acoustic pressure are shown. A continuous fluctuating signal is also noticed during the whole time-period (250 sec) of measurement that may be considered as the optical signature of the blood or other properties. During this time-period, a 1 MHz acoustic signal with 15 cycles per pulse has been induced after every 30 sec. Thus, a total of 9 shots of ultrasound pulses are targeted. For each pulse, when a shot of photo-acoustic signal is transmitted with a higher intensity of the laser beam, data has been collected and plotted. Thus, the observation of the bubble growth is observed after every 30 sec. This pulsating measurement technique also helps to avoid unwanted side-effects caused by a higher intensity of light and enable us to be imaging little deep. Acoustic pressure up to 333 kPa is non-destructive in nature for the microbubble, and growth of the micro-bubble is observed as an increment in the peak amplitude. However, if this pressure level is increased further, the inner shell (the core) of the bubble is collapsed, and leakage of gas started. This leakage in gas make the bubble dormant towards the acoustical pressure and thus further expansion in the bubble is ceased. This event is marked with the increment in the base fluctuating signal after 4 pulse. Therefore, a controlled diffusion in the gas become necessary to prevent the blood vessel to get ruptured. Therefore, corresponding to the cavitation threshold, pressure should be imposed on the micro-bubble.

To determine the cavitation threshold by the scattering of light, a micro-bubble having mean diameter has been considered as a reference bubble to characterize the growth of other individual bubbles. Thus, a non-linearity in the intensity of the scattered light is observed as compared to the reference scattering with the drift in the acoustic pressure towards the cavitation threshold. This non-linearity is caused, due to the asymmetric expansion in the bubble engender by the bursting of the inner shell of the bubble. Moreover, in context to the reference scattering of the light intensity, the size of the bubble can be estimated. Working in the direction of discrimination of the micro-bubbles. Therefore, authors classified the bubbles in two segments based on the reference diameter. Fig. 6 illustrated a scenario that represents the discrimination among the micro-bubble having different diameter compared to the reference diameter i.e. 5 µm in this case. One can easily distinguish the individual microbubble by observing the gap size presented between the spikes. This individual discrimination is based on the absorption of the light beam rather than the scattering of light. Therefore, whenever the bubble crosses the optical axis the peaks get extinction.

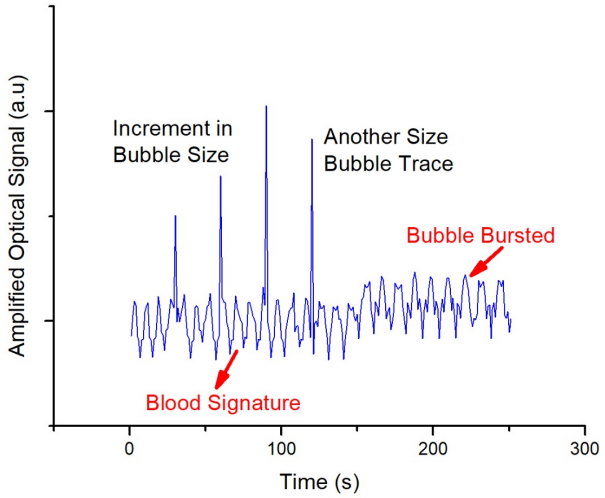

Fig. 5 Plot indicating the growth of the bubble after every shot of ultrasound signal. Fluctuating signals are also been reported in the plot, which may be considered as the signature of blood. Furthermore, bursting of microbubble is also recorded as the increment in the signal level.

This classification is necessary to understand the variation in the scattering pattern, as it is well known that the scattering is based upon the suspended particles. Thus, as the size of the microbubbles is increased, a unique scattering pattern will be observed in Fig. 6. This scattering pattern may further used to estimate the stretching in the outer lipid shell of the bubble, which in turn help to calculate the pressure level at the surface of the individual bubbles. Here, it is worth to note that the latency between the ultrasound pulses and the optical scattering creates ambiguity in the microbubble characterizations. So, to avoid this post-signal-processing issue it becomes necessary to achieve a high Signal to Noise Ratio (SNR). Hence, a high-intensity laser should be used with low noise detectors. Thus, it is envisioned that the PAFC type modelling for the characterization of microbubble dynamics have higher potential compared to other scattering based tools.

But still, there is a challenge to perform scanning in the large blood vessels because there is a trade-off between the beam width and the background noise. It may be possible that some bubbles, which are circulating in the blood vessel may get missed by the

laser beam. Therefore, this method is only suitable for the superficial blood vessels having small diameter so that a preferable optical environment (low tissue absorption) can be obtained. Furthermore, in case of deep sealed vessels, there is a high tissue absorption rate, hence scattered light intensity is attenuated largely, and optical resolution is reduced. Thus, it is concluded that, for superficial blood vessel, this method has the potential to characterize the micro-bubble dynamics, which allow monitoring the pressure level and cavitation threshold.

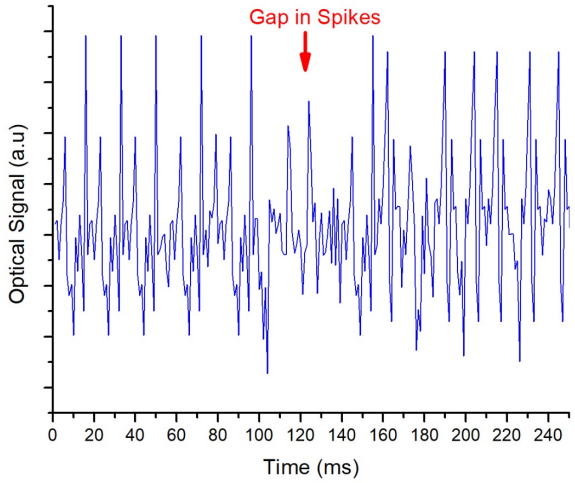

(a)

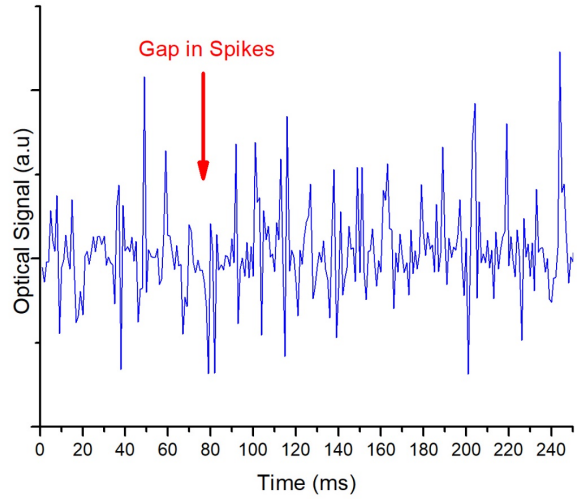

(b)

Fig. 6 Plots indicating the presence of microbubble having size (a) greater than 5 µm; (b) less than 5 µm. The size of the microbubble present at the foot print of the optical beam has been estimated by analysing the gap in the spikes.

Moreover, as we all are aware that only 10% of the antibiotics are consumed by the human body and rest 90% are excreted into the environment thereby affecting the ecosystem of the earth and sea creatures. Thus, by using such technique the optimum volume of drugs can be targeted towards the affected organ, that will not only reduce the recovery period of ailment but also minimize the side-effect on the other organs as well as the ecosystem. All the scientists and the researchers working on this field are contributing their baby-steps towards this new technique of drug delivery. However, epslon changes by each researcher will create a big impact in this direction. Finally, the authors have tried to contribute an epslon contribution in this side of research, although it is a drop-in ocean, authors hope that it will beneficial for all the researchers contributing in this direction.

5 Conclusion and Future Scope

A framework to characterize the dynamics of the micro-bubbles through analysing the intensity of the optical scattering by the PAFC system has been presented in this study. A multi-physics finite element method-based model is designed to examine the growth of the micro-bubbles under the influence of the acoustic pressure up to 333 kPa with 1 MHz frequency. The proposed model has indicated better efficacy in the case of the superficial blood vessel. Although, in the case of deep sealed blood vessels, authors have observed a reduction in the optical resolutions due to increment in the optical scattering losses. Another limitation of PAFC model is that the system only accounted for the microbubble that came into the vicinity of the laser. Although, most of the micro-bubbles, which are freely circulating in the vessel, remains out of the vicinity of the optical axis and did not contribute any optical scattering. In contrast, they have only produced most of the acoustic echoes and affecting the SNR of the model. However, authors have tried to improve the SNR by increasing the laser intensity level but faced the trade-off between different parameters. Therefore, this limitation of efficacy for deep sealed blood vessels and freely circulating microbubbles needs to be addressed in the future by increasing the SNR of the system or any other suitable technique. Despite above-mentioned constraints, the authors envisioned that the proposed model will provide low-cost, effective and less-complex estimation for characterization of the therapeutic micro-bubbles in case of superficial blood vessels. Furthermore, this technique unveils the secret of drug delivery that can help to reduce the side effects of medicine overdose.

Disclosures

All authors declare that there is no conflict of interests in this paper.

References

1. C. A. Sennoga, E. Kanbar, L.Auboire, P.-A. Dujardin, D. Fouan, J.-M. Escoffre, and A. Bouakaz, "Microbubble-mediated ultrasound drug-delivery and therapeutic monitoring," Expert Opinion on Drug Delivery 14(9), 1031–1043 (2017).
2. J. M Tsutsui, F. Xie, and R. T. Porter, "The use of microbubbles to target drug delivery," Cardiovascular Ultrasound 2(1), 23 (2004).
3. G. Shapiro, A. W. Wong, M. Bez, F. Yang, S. Tam, L. Even, D. Sheyn, S. Ben-David, W. Tawackoli, G. Pelled, K. W. Ferrara, and D. Gazit, "Multiparameter evaluation of in vivo gene delivery using ultrasound-guided, microbubble-enhanced sonoporation," Journal of Controlled Release 223, 157–164 (2016).
4. A. A. Doinikov, A. Bouakaz, "Modeling of the dynamics of microbubble contrast agents in ultrasonic medicine: Survey," Journal of Applied Mechanics and Technical Physics 54(6), 867–876 (2013).
5. J. E. Leeman, J. S. Kim, F. T. H. Yu, X. Chen, K. Kim, J. Wang, X. Chen, F. S. Villanueva, and J. J. Pacella, "Effect of Acoustic Conditions on Microbubble-Mediated Microvascular Sonothrombolysis," Ultrasound in Medicine & Biology 38(9), 1589–1598 (2012).
6. S. Datta, C.-C. Coussios, A. Y. Ammi, T. D. Mast, G. M. de Courten-Myers, and C. K. Holland, "Ultrasound-Enhanced Thrombolysis Using Definity® as a Cavitation Nucleation Agent," Ultrasound in Medicine & Biology 34(9), 1424–1433 (2008).
7. S. M. Chowdhury, T. Lee, and J. K. Willmann, "Ultrasound-guided drug delivery in cancer," Ultrasonography 36(3), 171–184 (2017).
8. F. Li, L. Wang, Y. Fan, and D. Li, "Simulation of noninvasive blood pressure estimation using ultrasound contrast agent microbubbles", IEEE Transactions on Ultrasonics, Ferroelectrics and Frequency Control 59(4), 715–726 (2012).
9. M. Postema, H. Abraham, O. Krejcar, and D. Assefa, "Size determination of microbubbles in optical microscopy: a best-case scenario," Optics Express 25(26), 33588 (2017).
10. S. Li, Y. Qin, X. Wang, and X. Yang, "Bubble growth in cylindrically-shaped optical absorbers during photo-mediated ultrasound therapy," Physics in Medicine & Biology 63(12), 125017.
11. C. Harfield, C. R. Fury, G. Memoli, P. Jones, N. Ovenden, and E. Stride, "Analysis of the Uncertainty in Microbubble Characterization," Ultrasound in Medicine & Biology 42(6), 1412–1418 (2016).
12. K. Efthymiou, N. Pelekasis, M. B. Butler, D. H. Thomas, and V. Sboros, "The effect of resonance on transient microbubble acoustic response: Experimental observations and numerical simulations," The Journal of the Acoustical Society of America 143(3), 1392–1406 (2018).
13. J. Sijl, B. Dollet, M. Overvelde, V. Garbin, T. Rozendal, N. de Jong, D. Lohse, and M. Versluis, "Subharmonic behavior of phospholipid-coated ultrasound contrast agent microbubbles," The Journal of the Acoustical Society of America 128(5), 3239–3252 (2010).
14. S. Paul, A. Katiyar, K. Sarkar, D. Chatterjee, W. T. Shi, and F. Forsberg, "Material characterization of the encapsulation of an ultrasound contrast microbubble and its subharmonic response: Strain-softening interfacial elasticity model," The Journal of the Acoustical Society of America 127(6), 3864–3857 (2010).
15. V. Garbin, D. Cojoc, E. Ferrari, E. Di Fabrizio, M. L. J. Overvelde, S. M. van der Meer, N. de Jong, D. Lohse, and M. Versluis, "Changes in microbubble dynamics near a boundary revealed by combined optical micromanipulation and high-speed imaging," Applied Physics Letters 90(11), 114103 (2007).
16. J. E. Chomas, P. A. Dayton, D. May, J. Allen, A. Klibanov, and K. Ferrara, "Optical observation of contrast agent destruction," Applied Physics Letters 77(7), 1056 (2000).
17. F. Urgiles, J. Perchoux, and T. Bosch, "Characterization of Acoustic Sources by Optical Feedback Interferometry," Proceedings 1(4), 348 (2017).
18. M. J. Hsu, M. Eghtedari, A. P. Goodwin, D. J. Hall, R. F. Mattrey, and S. C. Esener, "Characterization of individual ultrasound microbubble dynamics with a light-scattering system," Journal of Biomedical Optics 16(6), 067002 (2011).
19. J. F. Guan, T. J. Matula, "Using light scattering to measure the response of individual ultrasound contrast microbubbles subjected to pulsed ultrasound in vitro," The Journal of the Acoustical Society of America 116(5), 2832–2842 (2004).
20. E. I. Galanzha, V. P. Zharov, "Photoacoustic flow cytometry," Methods 55(3), 280–296, (2012).
21. M. A. Juratli, Y. A. Menyaev, M. Sarimollaoglu, A. V. Melerzanov, D. A. Nedosekin, W. C. Culp, J. Y. Suen, E. I. Galanzha, and V. P. Zharov, "Noninvasive label-free detection of circulating white and red blood clots in deep vessels with a focused photoacoustic probe," Biomedical Optics Express 9(11), 5667–5677 (2018).
22. D. Andrews, "Modelling of Ultrasonic Transducers and Ultrasonic Wave Propagation for Commercial Applications using Finite Elements with Experimental Visualization of Waves for Validation," Proceedings of the 2014 COMSOL Conference in Cambridge (2014).

23. E. I. Galanzha, M. G. Viegas, T. I. Malinsky, A. V. Melerzanov, M. A. Juratli, M. Sarimollaoglu, D. A. Nedosekin, and V. P. Zharov, "In vivo acoustic and photoacoustic focusing of circulating cells," Scientific Reports 6(1), 1–15 (2016).
24. M. A. Juratli, Y. A. Menyaev, M. Sarimollaoglu, E. R. Siegel, D. A. Nedosekin, J. Y. Suen, A. V. Melerzanov, T. A. Juratli, E. I. Galanzha, and V. P. Zharov, "Real-Time Label-Free Embolus Detection Using In Vivo Photoacoustic Flow Cytometry," PLOS One 11(5), e0156269 (2016).
25. L. C. Cabrelli, P. I. B. G. B. Pelissari, A. M. Deana, A. A. O. Carneiro, and T. Z. Pavan, "Stable phantom materials for ultrasound and optical imaging," Physics in Medicine and Biology 62(2), 432–447 (2017).
26. M. Kerker, The scattering of light and other electromagnetic radiation, Academic press, New York (1969).
27. F. M. Kahnert, "Numerical methods in electromagnetic scattering theory," Journal of Quantitative Spectroscopy and Radiative Transfer 79–80, 775–824 (2003).
28. T. Wriedt, "A Review of Elastic Light Scattering Theories," Particle & Particle Systems Characterization 15(2), 67–74 (1998).
29. V. Myroshnychenko, J. Rodríguez-Fernández, I. Pastoriza-Santos, A. M. Funston, C. Novo, P. Mulvaney, L. M. Liz-Marzán, and F. J. G. de Abajo, "Modelling the optical response of gold nanoparticles," Chemical Society Reviews 37(9), 1792–1805 (2008).
30. M. R. Rashidian Vaziri, A. Omidvar, B. Jaleh, and N. Partovi Shabestari, "Investigating the extrinsic size effect of palladium and gold spherical nanoparticles," Optical Materials 64, 413–420 (2017).
31. D. L. Kingsbury, P. L. Marston, "Mie scattering near the critical angle of bubbles in water," Journal of the Optical Society of America 71(3), 358 (1981).
32. M. A. Blizard, "Scattering Of Light By A Coated Bubble In Water Near The Critical And Brewster Scattering Angles," Proceeding of SPIE 925, 308 (1988).
33. L. Shi, L. A. Sordillo, A. Rodríguez-Contreras, and R. Alfano, "Transmission in near-infrared optical windows for deep brain imaging," Journal of Biophotonics 9(1–2), 38–43 (2016).
34. L. Hoff, P. C. Sontum, and J. M. Hovem, "Oscillations of polymeric microbubbles: Effect of the encapsulating shell," The Journal of the Acoustical Society of America 107(4), 2272–2280 (2000).
35. D. Chatterjee, K. Sarkar, "A Newtonian rheological model for the interface of microbubble contrast agents," Ultrasound in Medicine & Biology 29(12), 1749–1757 (2003).
36. H. Assadi, R. Karshafian, and A. Douplik, "Optical scattering properties of intralipid phantom in presence of encapsulated microbubbles," International Journal of Photoenergy 2014, 1–9 (2014).
37. J. Herbert, K. Bertling, T. Taimre, A. D. Rakić, and S. Wilson, "Microparticle discrimination using laser feedback interferometry," Optics Express 26(20), 25778 (2018).
38. J. Chen, K. S. Hunter, and R. Shandas, "Wave scattering from encapsulated microbubbles subject to high-frequency ultrasound: Contribution of higher-order scattering modes," The Journal of the Acoustical Society of America 126(4), 1766 (2009).
39. P. Marmottant, S. van der Meer, M. Emmer, M. Versluis, N. de Jong, and S. Hilgenfeldt, D. Lohse, "A model for large amplitude oscillations of coated bubbles accounting for buckling and rupture," The Journal of the Acoustical Society of America 118(6), 3499–3505 (2005).
40. G. L. Chahine, C.-T. Hsiao, "Modeling Microbubble Dynamics In Biomedical Applications," Journal of Hydrodynamics 24(2), 169–183 (2012).
41. J. M. Hyvelin, E. Gaud, M. Costa, A. Helbert, P. Bussat, T. Bettinger, and P. Frinking, "Characteristics and Echogenicity of Clinical Ultrasound Contrast Agents: An in Vitro and in Vivo Comparison Study," Journal of Ultrasound in Medicine 36(5), 941–953 (2017).
42. G. L. Chahine, "Interaction Between an Oscillating Bubble and a Free Surface," Journal of Fluids Engineering 99(4), 709–716 (1977).
43. A. N. Bashkatov, E. A. Genina, V. I. Kochubey, and V. V. Tuchin, "Optical properties of human skin, subcutaneous and mucous tissues in the wavelength range from 400 to 2000 nm," Journal of Physics D: Applied Physics 38(15), 2543–2555 (2005).